SANDIA REPORT
SAND2005-7105
Unlimited Release
Printed December 2005

Novel Catalysts for Hydrogen Fuel Cell Applications

Final Report (FY03–FY05)

Steven M. Thornberg, Eric N. Coker, William A. Steen, and Russell L. Jarek

Prepared by
Sandia National Laboratories
Albuquerque, New Mexico 87185 and Livermore, California 94550

Sandia is a multiprogram laboratory operated by Sandia Corporation,
a Lockheed Martin Company, for the United States Department of Energy's
National Nuclear Security Administration under Contract DE-AC04-94AL85000.

Sandia National Laboratories

Issued by Sandia National Laboratories, operated for the United States Department of Energy by Sandia Corporation.

Available to DOE and DOE contractors from
U.S. Department of Energy
Office of Scientific and Technical Information
P.O. Box 62
Oak Ridge, TN 37831

Telephone: (865) 576-8401
Facsimile: (865) 576-5728
E-Mail: reports@adonis.osti.gov
Online ordering: http://www.osti.gov/bridge

Available to the public from
U.S. Department of Commerce
National Technical Information Service
5285 Port Royal Rd.
Springfield, VA 22161

Telephone: (800) 553-6847
Facsimile: (703) 605-6900
E-Mail: orders@ntis.fedworld.gov
Online order: http://www.ntis.gov/help/ordermethods.asp?loc=7-4-0#online

SAND 2005-7105
Unlimited Release
Printed December 2005

Novel Catalysts for Hydrogen Fuel Cell Applications Final Report (FY03-FY05)

Steven M. Thornberg
Materials Reliability

Eric N. Coker
Ceramic Processing & Inorganic Materials

William A. Steen
Corrosion & Electrochemical Sciences

Russell L Jarek
YMP Repository Test & Analysis

Sandia National Laboratories
PO Box 5800, MS0889
Albuquerque, NM 87185

Abstract

The goal of this project was to develop novel hydrogen-oxidation electrocatalyst materials that contain reduced platinum content compared to traditional catalysts by developing flexible synthesis techniques to fabricate supported catalyst structures, and by verifying electrochemical performance in half cells and ultimately laboratory fuel cells. Synthesis methods were developed for making small, well-defined platinum clusters using zeolite hosts, ion exchange, and controlled calcination/reduction processes. Several factors influence cluster size, and clusters below 1 nm with narrow size distribution have been prepared. To enable electrochemical application, the zeolite pores were filled with electrically-conductive carbon *via* infiltratation with carbon precursors, polymerization/cross-linking, and pyrolysis under inert conditions. The zeolite host was then removed by acid washing, to leave a Pt/C electrocatalyst possessing quasi-zeolitic porosity and Pt clusters of well-controlled size. Plotting electrochemical activity *versus* pyrolysis temperature typically produces a Gaussian curve, with a peak at *ca.* 800 °C. The poorer relative performances at low and high temperature are due to low electrical conductivity of the carbon matrix, and loss of zeolitic structure combined with Pt sintering, respectively. Cluster sizes measured via adsorption-based methods were consistently larger than those observed by TEM and EXAFS, suggesting that a fraction of the clusters were inaccessible to the fluid phase. Detailed EXAFS analysis has been performed on selected catalysts and catalyst precursors to monitor trends in cluster size evolution, as well as oxidation states of Pt.

Experiments were conducted to probe the electroactive surface area of the Pt clusters. These Pt/C materials had as much as 110 m^2/g_{Pt} electroactive surface area, an almost *30% improvement* over what is commercially (mfg. by ETEK) available (86 m^2/g_{Pt}). These Pt/C materials also perform qualitatively as well as the ETEK material for the ORR, a non-trivial achievement. A fuel cell test showed that Pt/C outperformed the ETEK material by an *average of 50%* for a 300 hour test. Increasing surface area decreases the amount of Pt needed in a fuel cell, which translates into cost savings. Furthermore, the increased performance realized in the fuel cell test might ultimately mean less Pt is needed in a fuel cell; this again translates into cost savings. Finally, enhanced long-term stability is a key driver within the fuel cell community as improvements in this area must be realized before fuel cells find their way into the marketplace; these Pt/C materials hold great promise of enhanced stability over time.

An external laser desorption ion source was successfully installed on the existing Fourier transform ion-cyclotron resonance (FT-ICR) mass spectrometer. However, operation of this laser ablation source has only generated metal atom ions, no clusters have been found to date. It is believed that this is due to the design of the pulsed-nozzle/laser vaporization chamber. The final experimental configuration and design of the two source housings are described.

Table of Contents

Table of Figures

List of Tables

1. THE PREPARATION OF NOVEL PT/C ELECTROCATALYSTS WITH CONTROLLED POROSITY AND CLUSTER SIZE

1.1. Introduction

State-of-the-art electrocatalysts for Polymer Electrolyte Membrane Fuel Cells (PEM-FCs) rely on large quantities of platinum to achieve acceptable performance.[1] This presents a significant hurdle to market acceptance of FC-powered vehicles; a commercially viable electrocatalyst will require almost an order-of-magnitude reduction in Pt usage to meet both cost and Pt availability constraints. One avenue to reduce the amount of Pt required is through optimization of Pt cluster sizes for maximum electrochemical activity per unit mass, however, the interplay between maximizing Pt dispersion and size-specific reactivity needs to be better understood. The physical and chemical properties of nanoparticles of various elements are extremely sensitive to the number of atoms comprising the cluster when they contain less than a few dozen atoms. Furthermore, these variations in properties are often manifested in a non-linear fashion as the size of the cluster changes (1-6), and may be attributed to electronic and/or structural changes. The interaction of small clusters of atoms with the surface of a support may result in alteration of the electronic state of the cluster, depending on the nature of the support material.(7) There is some evidence that as the Pt cluster size reduces to below ~3nm electrochemical activity decreases,(8) however, large uncertainties exist due to the broad size distributions of most catalyst preparations analyzed in the literature. Direct measurement of the size-dependent properties of small Pt clusters with narrow size distribution would alleviate some uncertainties of size-dependent properties and enable design of optimized electrocatalysts for PEM-FCs. Established methods for the preparation of supported size-controlled metal clusters *via* colloid science and organometallic chemistry typically result in relatively large clusters (*i.e.*, >>1 nm)(9, 10). Deposition of neutral or ionic clusters from a laser vaporization source (e.g., "soft landing" approach) can be more successful at preparing small, size-selected supported clusters, but not in quantities sufficient for catalyst application.(11, 12) In the case of cluster deposition, the clusters are deposited from the gas phase onto the surface of a substrate such as carbon, yielding a thin-film catalyst material; Pt clusters with as small a size dispersion as 17% and with a mean size of 2.3nm have been obtained. Colloidal and organometallic approaches typically produce solubilized clusters, which must then be deposited onto or into a support matrix. Regalbuto, *et al.* have developed a procedure for preparing well-dispersed Pt on various support materials via electrostatic adsorption from solution.(13-16) Dispersions of Pt as high as 50% (~2nm clusters) were reported for 9.4wt.-%Pt-on-carbon (Vulcan XC-72) prepared using this method.(17)

Zeolites play host to noble metal clusters for numerous catalytic applications,(18-21) and well-defined clusters of narrow size distribution down to below 1nm may be obtained under suitable conditions.(22-26) However, due to their insulating characteristics, zeolite-supported clusters are not suitable as electrocatalysts. We have developed procedures whereby size-controlled Pt clusters in a zeolite could be rendered electrocatalytically active.(27, 28) This paper describes the process in detail, and discusses the factors governing cluster size control and electrochemical activity.

---

[1] Based on a state of the art electrocatalyst employing 0.5 g(Pt) kW^{-1}, a passenger vehicle would require ~25-50g Pt in its fuel cell; "Basic research needs for the hydrogen economy" Report of the Basic Energy Sciences Workshop on Hydrogen Production, Storage, and Use, May 13-15, 2003 [www.sc.doe.gov/bes/hydrogen.pdf].

1.2. Experimental Procedure

The zeolites used in this study were the commercially available, synthetic zeolite X (Aldrich Molecular Sieve 13X, powder), zeolite A (Aldrich Molecular Sieve 4A, powder), zeolite ZSM-5 (Zeolyst, Si/Al ~ 50, powder) and zeolite Beta (Zeolyst, Si/Al ~ 25, powder). In addition, a mesoporous silica material was synthesized in order to probe the effect of using a host with significantly larger pores than the zeolites. The majority of work was carried out using zeolite X, and the following description refers to this zeolite, but is applicable to all zeolite types. The Na-form of the zeolite was first converted to the Pt-form through direct aqueous ion exchange ($2Na^+ \leftrightarrow (NH_3)_4Pt^{2+}$) using the tetraammine nitrate salt $(NH_3)_4Pt(NO_3)_2$ (50.29 wt.-% Pt, Alfa Aesar). Platinum loadings were adjusted between 1 and 25 wt.-% (anhydrous, de-ammoniated basis) by varying the Pt-salt : zeolite mass ratio. The ion exchange of $(NH_3)_4Pt^{2+}$ into the zeolite was performed at low concentrations of Pt salt (typically 0.05M or less) in order to enhance selectivity for the divalent cation.(29) Due to the high selectivity of Na zeolite X (NaX) for $(NH_3)_4Pt^{2+}$ at low solution concentrations,(30) almost complete uptake of $(NH_3)_4Pt^{2+}$ from solution was found to occur when preparing the lower-loaded materials (up to 10 wt.-%). For the higher-loaded samples, excess Pt salt solution (still at low concentration) was used and multiple exchange reactions were sometimes required to reach high loadings, due to departure from stoichiometric $(NH_3)_4Pt^{2+}$ uptake. The $(NH_3)_4Pt^{2+}$-exchanged zeolite was then calcined in air to 350-400°C to decompose ("auto-reduce") the Pt complex and form partially-oxidized Pt clusters. These materials are referred to as [m]PtX(n:t), where m is the Pt-loading in wt.-% after calcination and dehydration, X denotes zeolite X, and n and t are the calcination heating rate in °C min^{-1} and the final calcination temperature in °C, respectively. The [m]PtX(n:t) was degassed under vacuum at a temperature between 80 and 120°C for several hours and then impregnated with an ethanolic solution of furfuryl alcohol (FFA, 99%, Across) while chilling in ice-water. Ethanol-to-FFA ratios were typically around 3:1, and the amount of FFA used was calculated to just fill the pore volume of the zeolite (assuming no pore blockage by Pt clusters), based on the pore volume of the parent zeolite as measured by the B.E.T. N_2-adsorption technique. After homogenizing the zeolite/FFA/ethanol slurry by a combination of stirring and ultrasonic agitation, the samples were placed under vacuum at room temperature in order to desorb excess solvent and draw the FFA into the pores of the zeolite. The sample was then heated in air to 80 – 120°C overnight to ensure complete polymerization of the FFA into poly-FFA (p-FFA). The [m]PtX(n:t)/p-FFA composite was then pyrolized under a flow of argon at between 400°C and 1200°C, with a two-hour isothermal hold at the ultimate temperature in a quartz glass tube furnace. In order to avoid oxidation of the carbonaceous material by trace oxygen in the inert gas stream, an O_2-getter furnace (Centorr Furnaces model 2B-20) was installed immediately upstream of the pyrolysis furnace, and an oxygen meter (Ametek TM1B oxygen analyzer) downstream of the furnace was used to verify the absence of oxygen and allow leak-detection. Materials prepared according to this procedure are referred to as [m]PtX(n:t)T, were T is the highest temperature reached during pyrolysis. During some preparations, two impregnation steps were performed, with an intermediate low-temperature pyrolysis step. In these instances, impregnation and polymerization were carried out as above, then the sample was pyrolized under inert at 400°C for one hour, cooled to room temperature, and the impregnation and polymerization repeated prior to the final pyrolysis treatment. These samples are referred to as [m]PtX(n:t)T/2*i*, where 2*i* represents two impregnation steps, with intermediate pyrolysis at 400°C. An optional pyrolysis treatment involved treatment under inert atmosphere to 400°C with a one-hour isothermal hold, then switching to a propylene-containing gas stream (0.75% propylene in N_2) and increasing the temperature to 800°C in order to decompose (pyrolize) the propylene in and on

the zeolite. Materials prepared according to this optional procedure are referred to as [m]PtX(n:t)T/pp, where pp denotes the in-situ deposition of propylene. During the post-pyrolysis cooling period, the inert atmosphere was replaced with 10% H_2 in N_2 in order to reduce the Pt to its metallic state. In the final stage of the process, the zeolite was removed by acid digestion using concentrated hydrofluoric acid at ambient temperature, leaving a conductive Pt/C electrocatalyst.

The Pt-loadings in the initial $Pt(NH_3)_4^+$-exchanged zeolites were determined by atomic absorption spectrophotometric measurement (AAS) of Pt concentrations in solution prior to and after the ion exchange reaction. Similarly AAS for Si, Al, Na, and Pt was used to monitor the amount of zeolite and platinum removed from the catalyst during the final HF washing procedure. The [m]PtX(n:t), Pt/C, and intermediate materials were characterized using a variety of techniques, including Transmission Electron Microscopy (TEM), X-ray powder Diffraction (XRD), Extended X-ray Absorption-Fine Structure (EXAFS), BET Surface Area analysis, chemisorption, thermo-gravimetric/differential thermal analysis (TGA/DTA) and ^{13}C Magic Angle Spinning Nuclear Magnetic Resonance Spectroscopy (MAS-NMR). Electrocatalyst evaluation has been performed using standard voltammetric techniques, including cyclic voltammetry, CO-stripping voltammetry, and Rotating Disk Electrode (RDE) evaluation of the Oxygen Reduction Reaction (ORR).

1.3. Results and Discussion

The general approach to preparing Pt/C electrocatalysts is summarized in simplified form in Figure 1, and each stage is discussed separately and in detail below. The preparation procedures for the samples discussed in this report are summarized in **Table** 1.

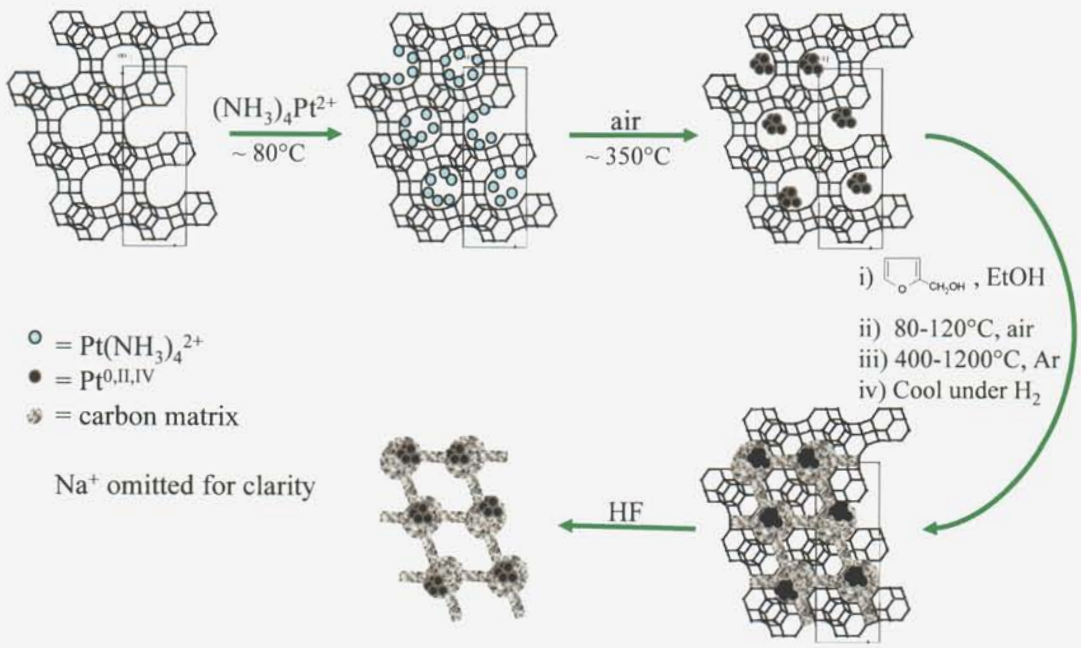

Figure 1. Simplified schematic of Pt/C electrocatalyst synthesis protocol, starting with a microporous host.

Table 1. Summary of preparation procedures for samples discussed in this report.

Sample number[1]	Pt-loading in zeolite (wt.-%)	Calcination rate (°C min^{-1}), temperature (°C)	FFA added (g g_{solid}^{-1})	Pyrolysis temperature (°C), conditions[2]	HF wash procedure[3]	Pt-loading in Pt/C (wt.-%)	Descriptor
1-26	20	2.0, 400					[20]PtX(2.0:400)
1-27A	20	2.0, 400	0.116				[20]PtX(2.0:400)/p-FFA
1-27AC	20	2.0, 400	0.116	600, N_2-H_2			[20]PtX(2.0:400)600/C
1-31A	20	0.1, 350					[20]PtX(0.1:350)
1-32A	20	0.1, 350	0	400, air (5°C min^{-1})			[20]PtX(0.1:350)400
1-41D2	5	2.0, 400					[5]PtX(2.0:400)
1-49A	11.5	0.1, 350					[11.5]PtSiO_2(0.1:350)
1-49B	11.5	1.0, 100 (air); 5.0, 250 (H_2)					[11.5]PtSiO_2(1.0:100-5.0:250)
1-55A	5	0.05, 350					[5]PtX(0.05:350)
1-55B	5	0.1, 350					[5]PtX(0.1:350)
1-55C	5	0.033, 350					[5]PtX(0.033:350)
1-58B	5	1.0, 350					[5]PtX(1.0:350)
1-63A	5	0.1, 350	0.440	400, N_2			[5]PtX(0.1:350)400/C
1-63B	5	0.1, 350	0.997	-			[5]PtX(0.1:350)400/C/p-FFA
1-63C	5	0.1, 350	0.997	400, N_2			[5]PtX(0.1:350)400/C/2*i*
1-65	5	0.1, 350	0.440	600, N_2; 600, pp			[5]PtX(0.1:350)600/C/pp
1-68	5	0.1, 350	0.997	800, N_2			[5]PtX(0.1:350)800/C
1-83	5	0.1, 350					[5]PtX(0.1:350)
2-54A	20.55	0.1, 350	0.398	800, pp	46.5% HF, o/n	47.68	[21]Pt(0.1:350)800/C/pp
2-54B	13.91	0.1, 350	0.395	800, pp	46.5% HF, o/n	38.32	[14]Pt(0.1:350)800/C/pp
2-54C	9.52	0.1, 350	0.397	800, pp	46.5% HF, o/n	20.46	[10]Pt(0.1:350)800/C/pp
2-54D	6.96	0.1, 350	0.395	800, pp	46.5% HF, o/n	16.82	[7]Pt(0.1:350)800/C/pp
2-54E	5.04	0.1, 350		800, pp	46.5% HF, o/n	12.21	[5]Pt(0.1:350)800/C/pp
2-54F	3.92	0.1, 350	0.404	800, pp	46.5% HF, o/n	9.72	[4]Pt(0.1:350)800/C/pp
2-54G	3.01	0.1, 350	0.400	800, pp	46.5% HF, o/n	7.84	[3]Pt(0.1:350)800/C/pp
2-54H	2.04	0.1, 350	0.397	800, pp	46.5% HF, o/n	6.55	[2]Pt(0.1:350)800/C/pp
2-54I	1.04	0.1, 350	0.401	800, pp	46.5% HF, o/n	3.63	[1]Pt(0.1:350)800/C/pp
2-61A	9.52	0.2, 350	0.408	800, pp	46.5% HF, o/n	21.22	[10]Pt(0.2:350)800/C/pp
2-61B	9.52	0.3, 350	0.407	800, pp	46.5% HF, o/n	25.93	[10]Pt(0.3:350)800/C/pp
2-61C	9.52	0.5, 350	0.418	800, pp	46.5% HF, o/n	28.35	[10]Pt(0.5:350)800/C/pp
2-61D	9.52	1.0, 350	0.404	800, pp	46.5% HF, o/n	22.70	[10]Pt(1:350)800/C/pp
2-61E	9.52	2.0, 350	0.422	800, pp	46.5% HF, o/n	29.11	[10]Pt(2:350)800/C/pp
2-61F	9.52	5.0, 350	0.405	800, pp	46.5% HF, o/n	29.28	[10]Pt(5:350)800/C/pp
3-28AB	20	0.1, 350					[20]PtX(0.1:350)
3-55Z	5	0.1, 350					[5]PtX(0.1:350)
3-56X	5	0.1, 350	0.440				[5]PtX(0.1:350)/p-FFA
3-57ZB	5	0.1, 350	0.382	400, N_2			[5]PtX(0.1:350)400/C
3-58B	10	0.1, 350					[10]PtX(0.1:350)
3-59ZB	5	0.1, 350	0.382	400, N_2	49% HF, 1.5hr	38.3	[5]Pt(0.1:350)400/C
3-85D	5	0.1, 350	0.629	900, N_2	49% HF, 36hr	77.0	[5]Pt(0.1:350)900/C
4-23A	2	0.1, 350					[2]PtA(0.1:350)

[1] All samples start with zeolite X except: 1-49A and 1-49B (mesoporous silica), and 4-23A (zeolite A).
[2] 800, pp = [m]PtX(n:t)/p-FFA pyrolized to 400°C, then 0.75% propylene/N_2 passed over catalyst while temperature ramped to 800°C.
[3] o/n = overnight.

1.4. Preparation of size-controlled Pt clusters stabilized in a zeolite matrix

The exchange of $(NH_3)_4Pt^{2+}$ cations into the zeolite was typically conducted at around 80°C in order to enhance the rate of ion exchange, and particularly to facilitate the stripping away of hydration water surrounding the Pt cations and thus allow their easier penetration into the channels of the zeolite. An analysis of the kinetics of the ion exchange reaction was not performed, and exchange reactions were allowed to proceed for a minimum of 8 hours. The concentration of Pt salt in solution was kept at, or below 0.05M, since high concentrations of the salt actually inhibit the ion exchange of the higher-valent cation when cations of unequal valency are competing for ion exchange sites.(29) Analysis via AAS of ion exchange supernatants after the exchange reaction had taken place showed that, for all solutions except those targeting the highest Pt-loadings (i.e., containing excess Pt salt), >99% of the Pt had been taken up by the zeolite.

The degree of Pt exchange (i.e., wt.-% Pt) has been found to influence the size of Pt clusters to a small degree, if all other processing variables are kept constant. EXAFS analysis of a suite of fully reduced samples [m]PtX(0.1:350), where m = 20, 10 and 5 wt.-% revealed a steady reduction in Pt-Pt coordination number (CN) as the Pt loading was reduced. The Pt-Pt CN is a function of the size of the cluster (provided any oxide is reduced prior to measurement). These data are summarized in Table 2, and the calculated cluster sizes are plotted in Figure 2. It was found that, after reduction in hydrogen at 250°C, platinum in all three catalysts was fully reduced. However, upon subsequent exposure to ambient air for 10 minutes, platinum in the two zeolites with the lower Pt-loadings was fully oxidized (all Pt atoms accessible to air), while that in the high-loaded zeolite was only partially oxidized, even after extended exposure to air. This indicated that the clusters in the high-loaded zeolite were sufficiently large to possess an "inner core" of Pt atoms inaccessible to the gas phase.

Table 2. Summary of EXAFS data for Pt-zeolite X samples with varying Pt loading, calcined at a limiting ramp rate of 0.1 °C min-1.

Sample	Pt-loading / wt.-%	Sample descriptor	Pt-Pt CN
3-55Z	5	[5]PtX(0.1:350)	6.1
3-58B	10	[10]PtX(0.1:350)	7.1
3-28AB	20	[20]PtX(0.1:350)	7.7

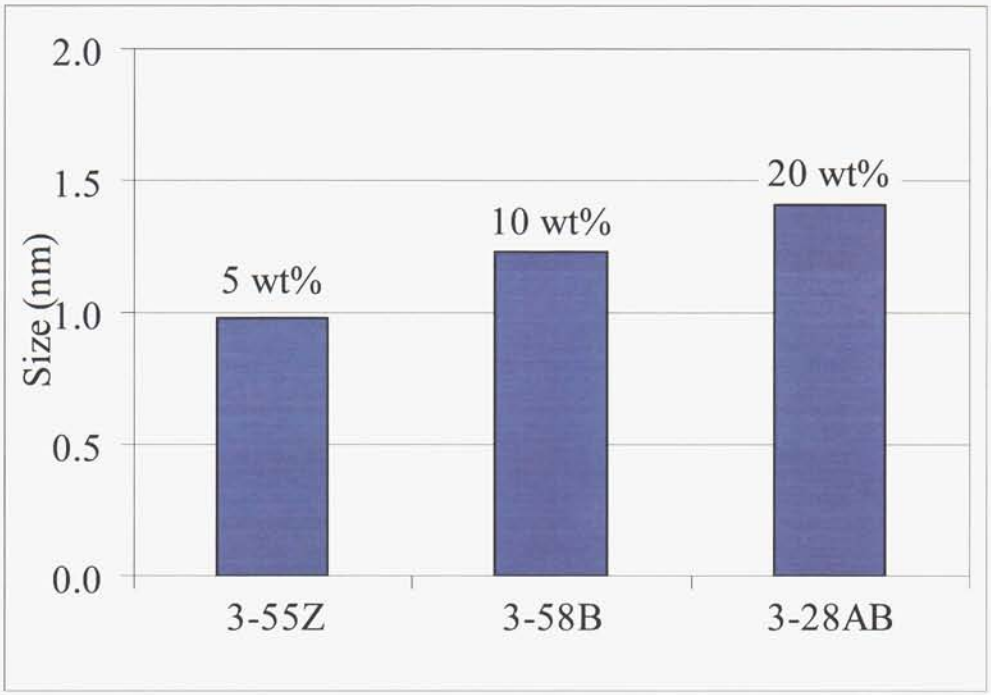

Figure 2. Variation in calculated Pt cluster size with Pt loading. All samples were calcined at a limiting rate of 0.1°C min^{-1}. Calculations in accordance with Ref. 22 based on bulk Pt-Pt coordination numbers from EXAFS measurements.

Further control over cluster size may be garnered by adjusting the rate of ramping the temperature during initial calcination of [m]PtX(n:t), as described elsewhere.(22-25) Figure 3 shows TEM images of a range of 5wt.-% Pt zeolite X samples calcined at limiting rates (n) between 0.033 and 2.0 °C min^{-1}. In all cases, Pt clusters of the order of 1 nm were obtained, (i.e., small enough to reside within the supercages of the zeolite structure) and the differences between samples are quite subtle. Thorough examination of a series of images of each sample lead to the general observation that for $n > 0.5$°C min^{-1}, cluster size monodispersity is compromised, while no significant cluster size decrease is realized for $n < 0.1$°C min^{-1}. Some quantitative results were obtained from EXAFS, and the Pt-Pt coordination numbers (CN) and other pertinent data are summarized in Table 3. The Pt-Pt CNs for samples with $0.05 < n < 1.0$°C min^{-1} are essentially identical, while the sample calcined at 0.033°C min^{-1} had a significantly larger CN (meaning, larger clusters). This may be explained by the fact that, at a rate of 0.033°C min^{-1}, the sample spent 25 hours between 300 and 350°C, which may have been long enough for cluster migration and agglomeration to become significant. As a result of this data, a limiting calcination ramp rate of 0.1 °C min^{-1} was adopted as standard. The XRD powder patterns of these materials showed no Pt metal (due to the clusters being too small to diffract X-rays coherently) and zeolite fingerprints were similar to the un-calcined materials.

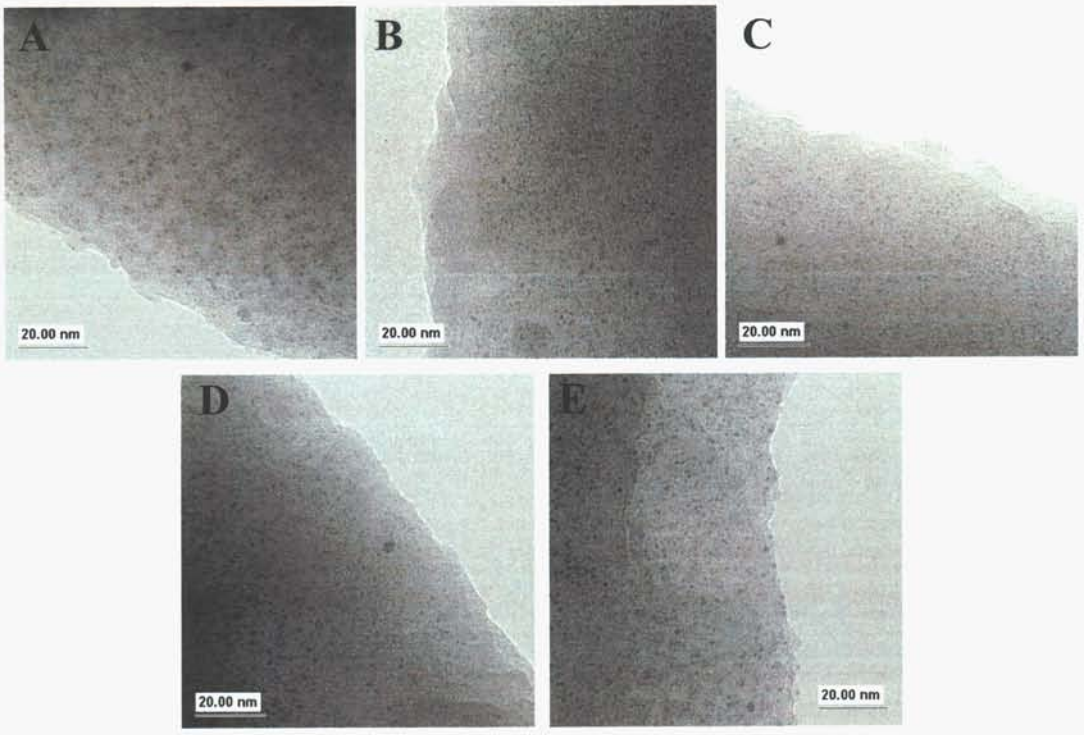

Figure 3. Examples of zeolite-supported Pt clusters formed as a function of limiting calcination ramp rate (n). All samples contain 5 wt.-% Pt in zeolite X. A: sample 1-55C, n = 0.033°C min^{-1}; B: sample 1-55A, n = 0.05°C min^{-1}; C: sample 1-55B, n = 0.1°C min^{-1}; D: sample 1-58B, n = 1.0°C min^{-1}; sample 1-41D2, n = 2.0°C min^{-1}.

Table 3. Summary of EXAFS data for Pt-zeolite X samples calcined at various ramp rates.

Sample	Limiting ramp rate (n) / °C min^{-1}	Sample descriptor	Pt-Pt CN
1-55C	0.033	[5]PtX(0.033:350)	6.4
1-55A	0.05	[5]PtX(0.05:350)	6.0
1-55B	0.1	[5]PtX(0.1:350)	6.1
1-58B	1	[5]PtX(1.0:350)	5.9

Beside the calcination rate, the degree of hydration of the zeolite prior to calcination can have a profound influence on the Pt cluster size, especially at the higher ramp rates (i.e., n > 1°C min^{-1}). Each of the samples in Figure 3 and Table 3 was thoroughly dried prior to calcination. However, sample 1-26, [20]PtX(2:400) shown in Figure 4 was dried only briefly, and contained excess water of hydration prior to calcination. The resulting Pt-clusters possessed a broad distribution of sizes, mostly between 3 and 6 nm in diameter. Powder XRD clearly identified Pt metal after calcination in air, while the diffraction peaks for the zeolite had degraded somewhat compared to its Pt-exchanged predecessor. The higher Pt loading in this sample is not sufficient to account for the dramatic increase in cluster size compared to [5]PtX(2:350) shown in Figure 2, and the elevated final temperature is not responsible (sample [5]PtX(1:400) is indistinguishable from [5]PtX(1:350), not shown).

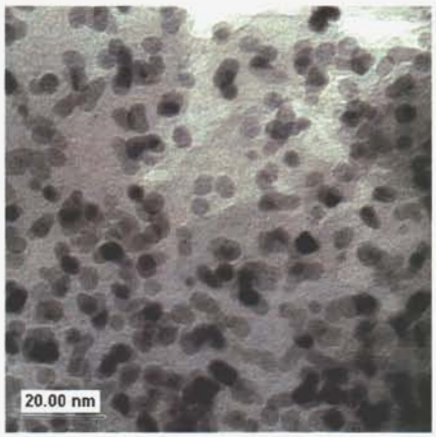

Figure 4. Pt clusters in [20]PtX(2:400) obtained on calcination of highly hydrated zeolite.

The dependence of cluster size on ramp rate and level of hydration may be explained by considering the high affinity the zeolite displays toward both water and ammonia; both diffuse out of the zeolitic pores only slowly. On the other hand, the presence of water and ammonia ligands enhances the mobility of Pt species at temperatures above 300°C. By heating the sample at a slow rate, water and ammonia (originating from pore-filling water and Pt-salt decomposition, respectively) have time to diffuse out of the zeolite before sufficiently high temperatures are reached, at which Pt mobility would be an issue. In support of this proposition, it has also been observed that samples which possess excess moisture prior to calcination exhibit a stronger dependence of Pt cluster size on ramp rate than those which are dried thoroughly. The majority of samples discussed here were therefore dried under vacuum prior to calcination. Analysis of the decomposition of $Pt(NH_3)_4^{2+}$ via TGA/DTA showed weight losses attributed to the ammonia ligands between 300 and 350°C. Subsequent experimentation revealed that the rate (between 0.1 and 2°C min^{-1}) at which the sample was heated to 300°C had a negligible effect on the ultimate cluster sizes, but the heating rate from 300°C to the final temperature was critical. Thus, samples were typically heated at ~2°C min^{-1} to 300°C, and the rate used above 300°C was defined as the "limiting rate" (n).

The size of Pt clusters is influenced to some degree by the size of the cavities and channels in the zeolite host, provided appropriate calcination conditions are employed. This fact is illustrated in Figure 5, where TEM images of various $Pt(NH_3)_4^{2+}$-exchanged micro- and meso-porous hosts calcined under the same conditions are compared. The two microporous hosts possessed Pt loadings ~ 5 wt.-%, and the mesoporous silica contained ~10wt.-% Pt. All three were prepared with a limiting calcination rate of 0.1°C min^{-1}. Although the differences in cluster sizes between these different materials has not been quantified, a qualitative assessment of the TEM images shows that the small-pore zeolite A (0.41 nm window, 1.1 nm cavity) shown in Figure 5A contains the smallest clusters (sample 4-23A), while the meso-porous SBA-15 (channels ~ 5.6 nm), Figure 5C, contains by far the largest clusters (sample 1-49A). The medium pore-size zeolite X (0.74 nm pore window, 1.3 nm cavity), Figure 5B (sample 1-83), possesses intermediate sized clusters, slightly larger than those seen in zeolite A. The mesoporous host clearly resulted in poor control of the cluster growth under these conditions. Using modified conditions (1^{st}: calcination overnight in air at 100°C, ramp rate 1°C min^{-1}; 2^{nd}: reduction under H_2 for two hours at 250°C, ramp rate 5°C min^{-1}), better control over cluster sizes was achieved using the mesoporous host, as shown in Figure 5D (sample 1-

49B). In the latter sample, Pt cluster sizes are almost as small as those obtained in the zeolites.

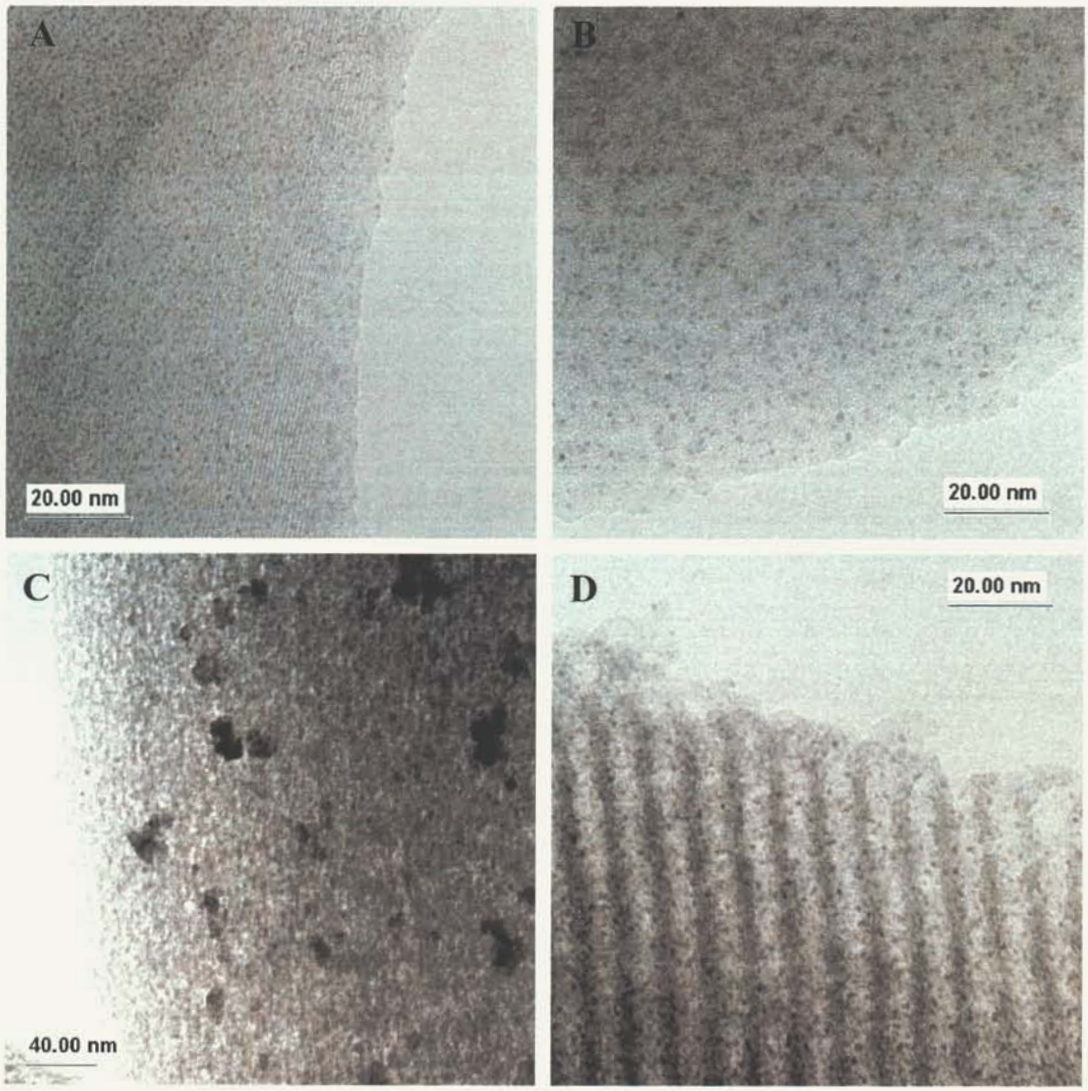

Figure 5. TEM images of Pt clusters supported on various micro- and meso-porous materials. A: 5 wt.-% Pt on zeolite A, [5]PtA(0.1:350); B: 5 wt.-% Pt on zeolite X, [5]PtX(0.1:350); C: 10 wt.-% Pt on mesoporous silica, [10]PtSiO2(0.1:350); D: 10 wt.-% Pt on mesoporous silica, prepared by modified route (see text).

Once the Pt clusters have been formed, they have proven to be quite stable to temperatures up to 400°C. This is demonstrated in Figure 6, which shows: A) sample 1-31A, freshly-prepared [20]PtX(0.1:350), and B) the same material after it was re-heated in air to 400°C at a fast heating rate of 5°C min^{-1} (sample 1-32A). There is no significant difference observable between the two samples. The limit of this stability has not been determined, but is below 600°C (*vide infra*).

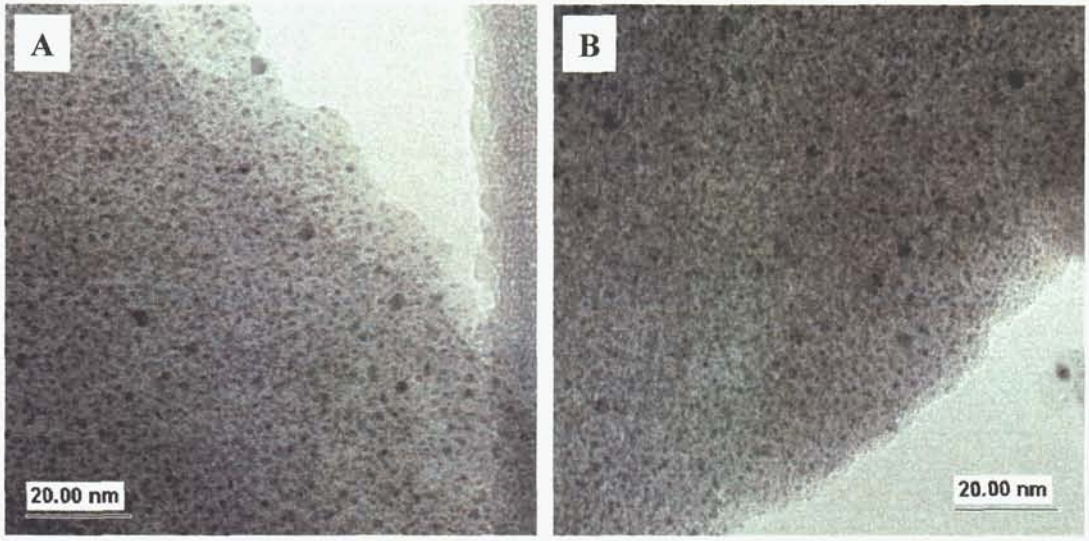

Figure 6. Demonstration of stability of Pt clusters to moderate temperature treatment. A: parent material calcined at 0.1 °C min-1, [20]PtX(0.1:350); B: same material after rapid heating (5 °C min-1) in air to 400 °C.

Many of the early Pt-cluster containing samples prepared were found by TEM to possess bi-modal cluster size distributions. Besides the smaller, controlled clusters, there was often a small population of larger clusters between 2 and 4nm in diameter (several of these larger particles are prominent in Figure 6). These large clusters are believed to reside at the outer surface of the zeolite crystals or at large crystal defects, where they can grow without the restriction of controlled zeolitic porosity. Various techniques were employed in attempts to prevent their occurrence, or remove them after formation, as described below. The simplest process used to reduce the occurrence of large clusters was to increase the extent of washing at the end of the ion exchange reaction in order to remove any loosely-bound $(NH_3)_4Pt^{2+}$ at or near the outer surface of the zeolite crystallites. A variation on this process was to wash the $(NH_3)_4Pt^{2+}$-exchanged material with a solution of tetra-pentyl ammonium chloride (TPACl) in an attempt to remove surface and near-surface Pt species by ion exchange ($(NH_3)_4Pt^{2+} \leftrightarrow 2TPA^+$). The TPA^+ cations are too large to enter the pores of the zeolite, therefore replace only those Pt cations at the surface of the crystallite. A literature procedure for the dissolution of Pt clusters was used in an attempt to remove any clusters on the outer surface of the zeolite.(31) This process involved refluxing the Pt-cluster/zeolite sample in a solution of tetrapropyl ammonium bromide and bromine in acetonitrile for four hours, followed by further refluxing in acetonitrile to wash sample. TEM images showed a modest reduction in the number of large Pt particles, while elemental analysis showed ~ 1% of Pt had been removed.

Of the procedures noted above for avoidance of large Pt clusters, simple extended washing of samples at the end of the ion exchange reaction was used for the samples described in this paper, unless otherwise noted.

1.5. Generation of secondary carbon matrix

In order to allow infiltration of the Pt-zeolite pore volume by furfuryl alcohol (FFA), a minimum pore opening of ~ 0.5 nm is required (i.e., kinetic diameter of FFA ~ 0.5 nm). Zeolite A, therefore, was not a suitable candidate for generation of a secondary carbon matrix

using FFA. Zeolite X, with 0.74 nm pore openings was used for the majority of this work. Once the size-controlled clusters had been prepared as described in section 3.1, [m]PtX(n:t) was activated at moderate temperature (typically 120°C, vacuum) to remove the bulk of the water and other pore-filling species, while not heating high enough to mobilize the clusters and cause sintering (earlier experiments showed the clusters to be stable to at least 400°C, *vide supra*). On contacting the solid with the FFA solution in air, an exothermic reaction was observed to occur, sometimes accompanied by spontaneous combustion. In order to prevent ignition, it was found sufficient to cool the zeolite samples and FFA solution in ice water prior to and during mixing. After homogenizing by a combination of mixing and ultrasonic agitation, the paste was placed under vacuum to draw the FFA into the zeolite pores and remove additional solvent. The vapor pressure of FFA is low at room temperature, and negligible loss of monomer was expected on evacuation. Once a damp or incipiently wet paste was obtained, the sample was removed from the vacuum and homogenized thoroughly. The sample was then placed in an oven at 80°C for two to four hours, then the temperature was raised to 120°C and left for a minimum of four hours to ensure complete polymerization of the FFA into poly-FFA (p-FFA). This was usually accompanied by a slight darkening of the sample. The polymerization reaction results in cross-linking of the FFA molecules into linear chains (Figure 7). That three-dimensional cross-linking does not occur to a significant degree is supported by the poor rigidity of the polymer matrix prior to pyrolysis. TEM images of zeolite/p-FFA samples (with or without Pt) before and after HF treatment show that the morphology of the zeolite is lost after HF treatment, and that the polymer network is not rigid.

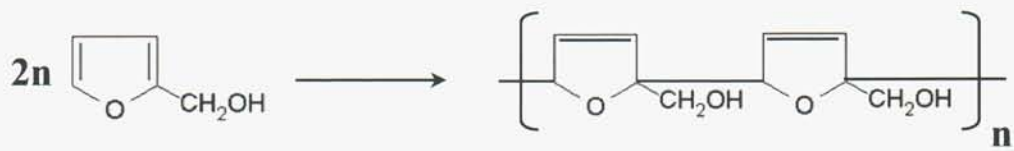

Figure 7. Depiction of reaction occurring during polymerization of furfuryl alcohol (FFA).

The pyrolysis protocol of [m]PtX(n:t)/p-FFA is undoubtedly one of the major controlling factors in whether a good electrocatalyst is achieved. A study was carried out into the effect of varying the temperature of pyrolysis, where a sample of pure p-FFA was subjected to various pyrolysis treatments prior to measuring electrical resistivity with a simple voltmeter test. The results of these tests are shown in Figure 8, and it can be seen that electrical conductivity for a 400°C-pyrolized sample was negligible, but rose steadily as the pyrolysis temperature was increased to 1000°C. A large jump in conductivity was noticed between samples pyrolyzed at 1000 and 1200°C. Thermogravimetric and differential thermal analysis (TGA/DTA) of the pure p-FFA between room temperature and 1200°C under inert atmosphere superimposed on the conductivity data, Figure 8, showed that weight loss was complete around 900°C, while a re-structuring of the carbon occurred at around 1050°C (endotherm with no associated weight change). It is this re-structuring which accounts for the relatively high conductivity in the 1200°C-pyrolized material. The total weight lost under the inert pyrolysis conditions simulated in the TGA/DTA is 50 wt.-%, corresponding closely to that calculated assuming all H atoms are given off as H_2, and all O atoms as CO_2 (see Appendix A for more details).

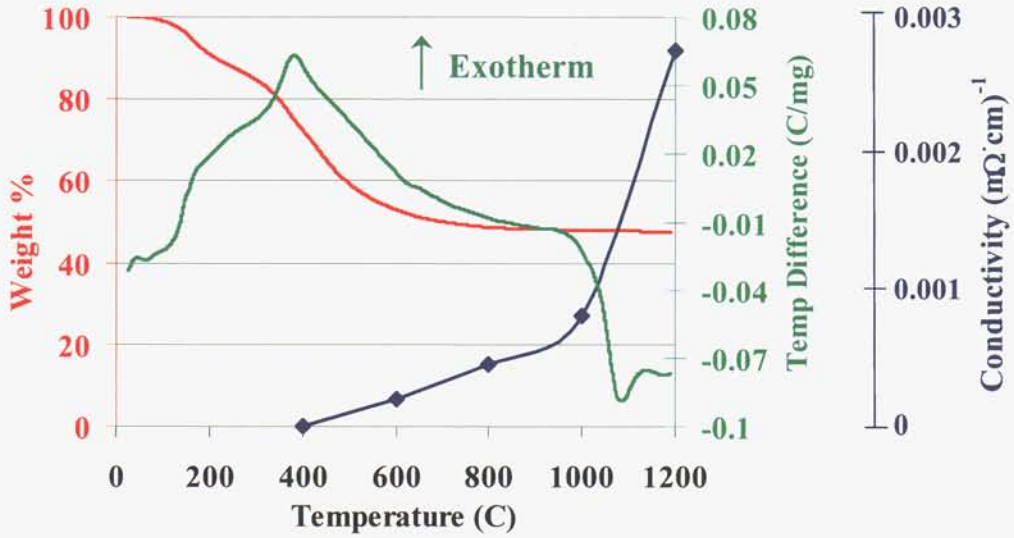

Figure 8. Conductivity measurements on pure p-FFA pyrolized to various temperatures, and TGA/DTA traces for p-FFA heated under inert atmosphere from ambient to 1200°C.

Alternative pyrolyisis methods have also been investigated, including two-stage impregnation, and impregnation followed by in-situ propylene decomposition. The rationale behind these two approaches is that, as the p-FFA undergoes pyrolysis, its volume shrinks, with the possibility of opening fissures which allow Pt clusters to migrate more easily, and also potentially reducing the Pt-carbon interface area and thus reducing electronic conduction. The two techniques investigated provide means to partially re-fill the volume realized by p-FFA densification, with the aims of enhancing catalyst durability and electronic conductivity. In the two-stage impregnation process, the FFA-impregnated and polymerized sample was pyrolized for 2 hours at 400°C in order to densify the organic component and release the majority of H_2 and CO_2. A second impregnation was then carried out under ambient conditions, using the same amount of FFA as in the original impregnation. Pyrolysis of this material was then carried out at between 600 and 800°C in order to carbonize the organic fraction completely. TGA/DTA analysis of a series of samples taken at stages throughout this process showed the change in combustible mass of the sample, and the changes in combustion exotherm (both intensity and light-off temperature), as illustrated in Figure **9.** After the first FFA impregnation and pyrolysis at 400°C, ~ 26% weight loss was recorded with an intense exothermic peak in the DTA at ~330°C, as well as a broad exotherm at ~460°C, while after the second impregnation, but before pyrolysis, the weight loss increased to ~32%, mainly due to the loss of p-FFA at low temperature (broad exothermic event at around 200°C in DTA trace). After pyrolysis of this material at 400 °C, the weight loss decreased to ~30%, due to the partial densification of the polymer during pyrolysis (loss of some H_2 and CO_2). The DTA trace of this sample was almost identical to that of the once-impregnated and pyrolized material. After pyrolyzing the material at 800°C, a smaller combustible fraction remained (~12%), indicating further, more substantial loss of H_2 and CO_2 from the polymer. The DTA profile of the 800°C-pyrolized sample was significantly different from the earlier ones, and two relatively low intensity exotherms occurred at ~425 and 578°C, corresponding to the two major weight loss events.

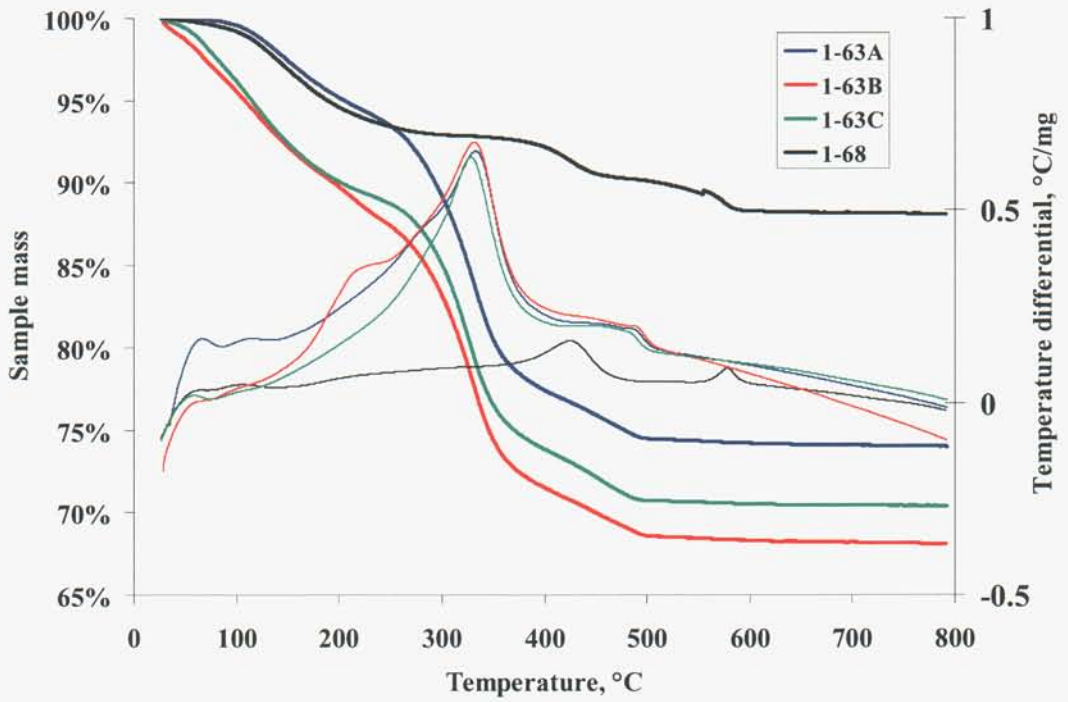

Figure 9. TGA/DTA analysis of [5]PtX(0.1:350)/p-FFA (parent = sample 3-56X) pyrolized at 400°C (1-63A); after a second FFA-impregnation and polymerization, but before the second pyrolysis (1-63B); after the second pyrolysis at 400°C (1-63C); and the same sample after pyrolysis at 800°C (1-68). Thick lines = sample mass fraction (TGA); thin lines = temperature differential (DTA).

For the propylene deposition process, Figure 10 shows the TGA/DTA profiles for a typical preparation sequence. A Pt zeolite which had been impregnated with FFA and polymerized (sample 3-56X) showed a weight loss of 35% with an exotherm centered at 220°C; after 600°C pyrolysis, the weight loss decreased to ~29% and the exotherm moved to ~350°C (sample 3-56X, pyr. 600°C). A separate sample of 3-56X was subjected to pyrolysis at 600°C followed by in-situ propylene deposition at 600°C for one hour (sample 1-65). The TGA/DTA profile of this sample showed a weight loss of 25%, with an intense, sharp exotherm occurring at 300°C, as well as two minor, broad exotherms which correspond closely to those seen in the sample pyrolized at 600 °C without propylene deposition (3-56X, pyr. 600°C). Clearly the sharp exotherm at 300°C and corresponding mass loss are due to the in-situ deposited carbon from propylene pyrolysis.

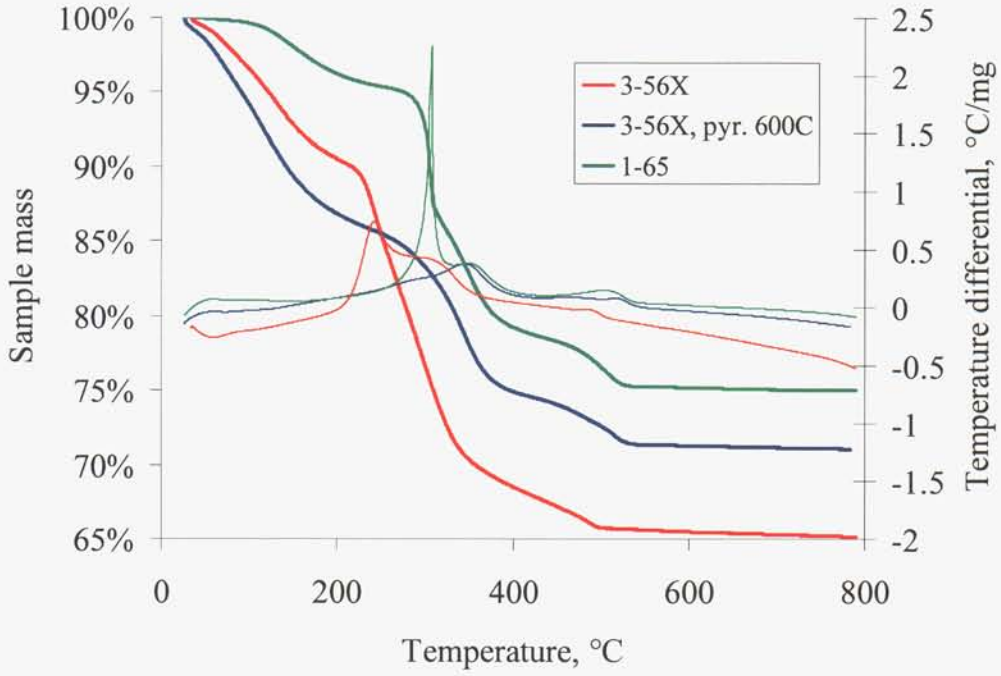

Figure 10. TGA/DTA analysis of [5]PtX(0.1:350)/p-FFA before pyrolysis (3-56X); after pyrolysis at 600°C (3-56X, pyr. 600°C); and a separate sample of 3-56X which had been partially pyrolized at 600°C, then exposed to a propylene-containing gas stream at 600°C, and held for 1 hour (1-65). Thick lines = sample mass fraction (TGA); thin lines = temperature differential (DTA).

A study was conducted of various alternative carbon precursors, and methods of generating the carbon matrix. Alternative carbon sources were chosen from the sugars (fructose, sucrose, glucose, galactose and lactose). In order to simplify the analysis, Pt-free zeolites were used as hosts, and a simple measurement of electrical resistance across a pressed disc of material was used as the metric. In parallel with the sugars, zeolites containing p-FFA, and p-FFA with in-situ propylene pyrolized at 800°C were included in the study. For these experiments, sugar impregnation was similar to that described for FFA, using aqueous solutions, and pyrolysis was performed over a range of temperatures. Digestion of the zeolite was accomplished using HF treatment. The list of sugars was down-selected to fructose and sucrose after a few preliminary experiments. A comparison of the resistances of the various prepared carbons is given in Figure 11; the resistance of commercially available Vulcan XC-72 carbon, measured in the same way as the sugar-derived carbons, is shown for comparison (as a solid line independent of temperature). The two sugars develop conductivity at temperatures well below p-FFA, but do not achieve the conductivity of XC-72 carbon until 1000°C. The p-FFA approaches the conductivity of the sugars only once pyrolized to 1000°C. In contrast, the propylene-modified p-FFA (p-FFA/pp) follows the conductivity of the sugars, and achieves a resistance only 2 – 2.5 times that of XC-72 between 800 and 900°C.

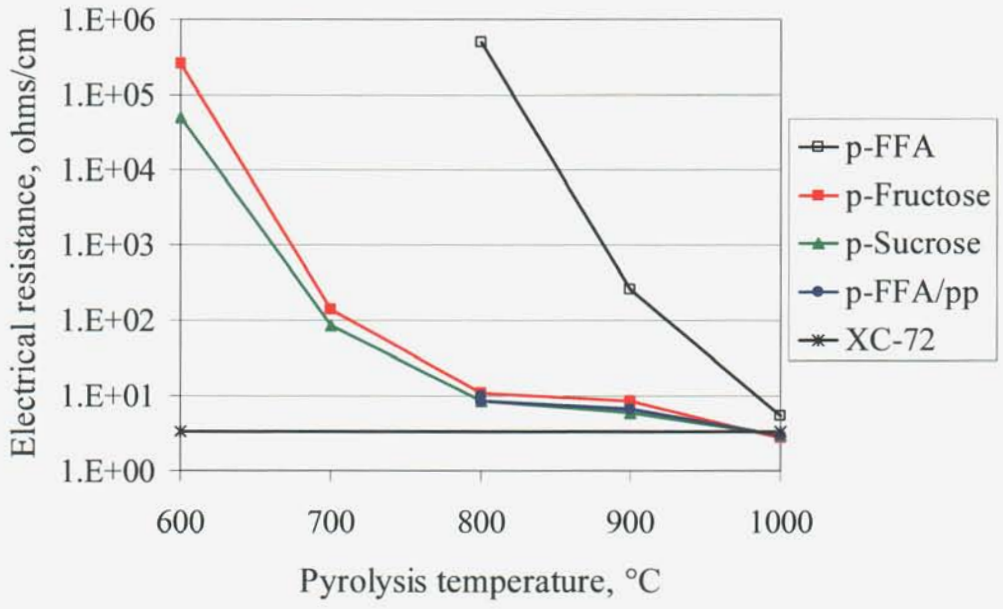

Figure 11. Electrical resistance of pyrolized carbon precursors as a function of pyrolysis temperature. For comparison, commercial Vulcan XC-72 carbon is represented as a temperature-independent line.

Pyrolysis of the p-FFA containing samples (with or without propylene deposition) resulted in a color transition from brown to black, while solid state ^{13}C NMR revealed a transition from mostly sp^3 carbon in p-FFA to mostly sp^2 carbon after pyrolysis, as shown in Figure 12. Note that sp^2-hybridized carbon is the graphitic form responsible for electrical conductivity.

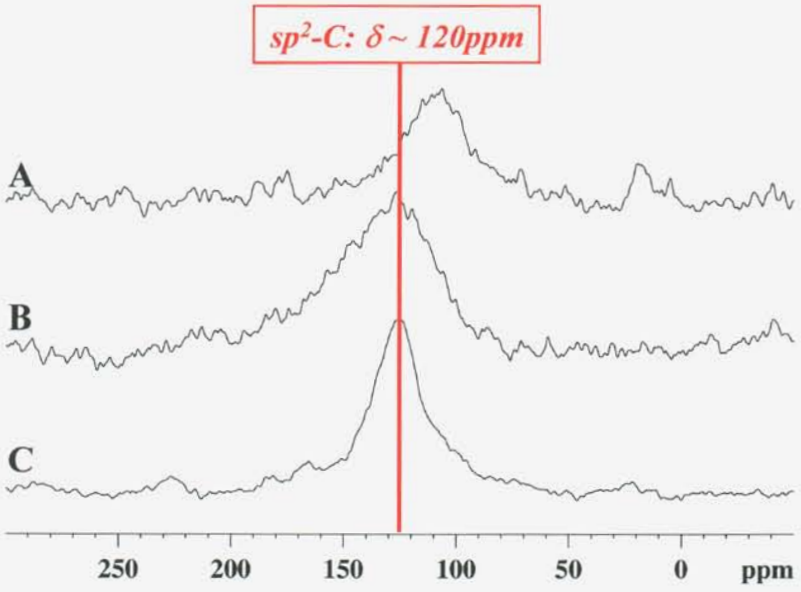

Figure 12. ^{13}C MAS NMR spectra for [20]PtX(2:400)/p-FFA before (A), and after (B) pyrolysis at 600°C. A commercial 10% Pt/carbon catalyst from Alfa Aesar is shown for comparison (C).

The presence of the polymer/carbon matrix within the pores of the Pt zeolite helps to stabilize the Pt clusters against sintering at high temperatures. While it was demonstrated earlier (Figure 6), that the zeolite-supported clusters are stable to at least 400°C, the presence of the carbonaceous material extends that stability to ~600°C. Figure 13 shows TEM images of A: [20]PtX(1:350), B: [20]PtX(1:350) after heating under inert atmosphere to 600°C, and C: [20]PtX(1:350)/p-FFA after heating under inert atmosphere to 600°C. On treatment under pyrolysis conditions, the Pt clusters in the sample without polymer (B) grew to ~ twice the diameter (eight times the mass) of the parent material (A), while the polymer-containing sample (C) underwent only mild sintering. Approximate cluster size ranges determined from the TEM images are indicated.

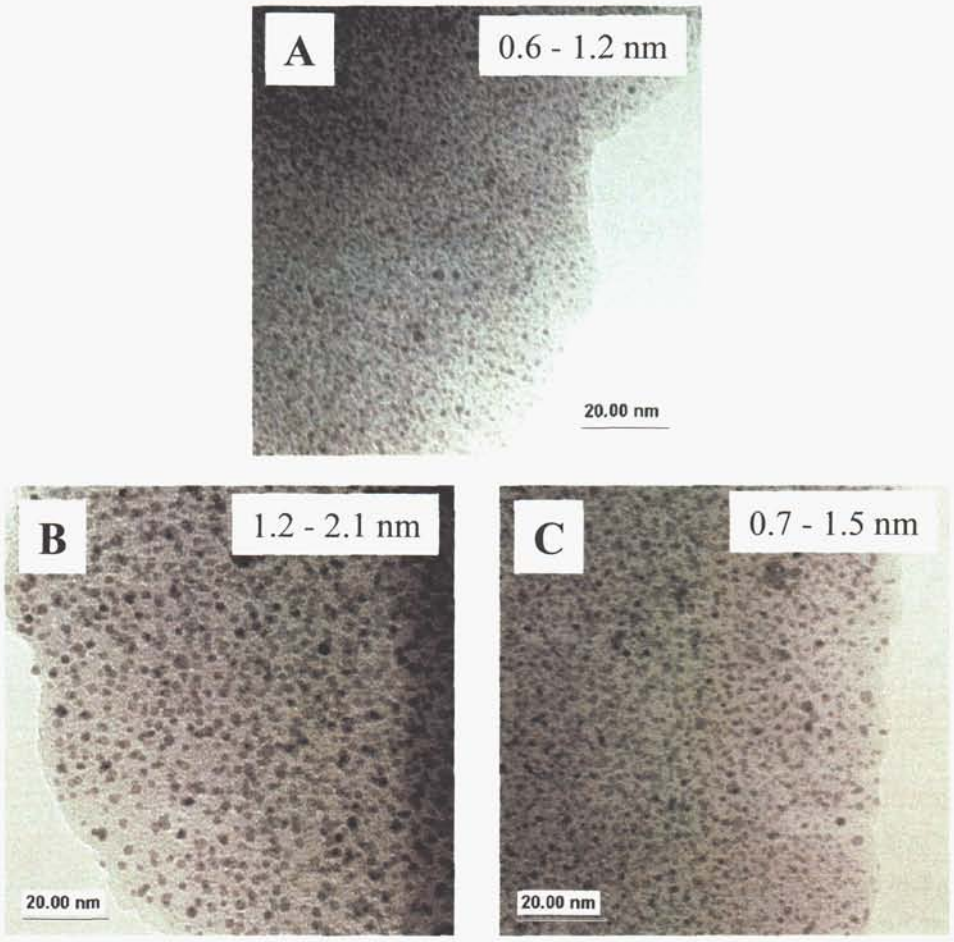

Figure 13. Demonstration of cluster stability in the presence of the secondary carbonaceous matrix. A: sample [20]PtX(1:350); B: sample [20]PtX(1:350) after 600 °C pyrolysis; C: sample [20]PtX(1:350)/p-FFA after 600 °C pyrolysis.

1.6. Digestion of zeolite

In the final stage of the procedure, the carbon-containing PtX materials were treated with hydrofluoric acid (HF) in order to release the Pt/C electrocatalyst. An evaluation of different digestion protocols revealed that soaking in concentrated HF at room temperature for a few hours was sufficient to remove essentially all of the zeolite components (Si, Al, Na and O). Digestion using basic solution (e.g., NaOH), or with dilute HF or other acids gave poor

reproducibility, and generally left larger amounts of residual inorganic components in the final electrocatalyst.

Analysis of the post-digestion supernatant solution by AAS showed that only a small fraction of the Pt was lost during the treatment (<<1% of Pt present), and that the amounts of Si, Al and Na released were in agreement with expected levels assuming all of the zeolite was dissolved. Comparison of bulk cluster sizes by EXAFS for samples before and after HF-treatment revealed an unexpected increase in cluster size after HF treatment (see Figure 14). The reason for this change is not fully understood, but may be partly due to the selective dissolution in HF of some of the smallest clusters, resulting in an increase in the average size of clusters, as measured by EXAFS.

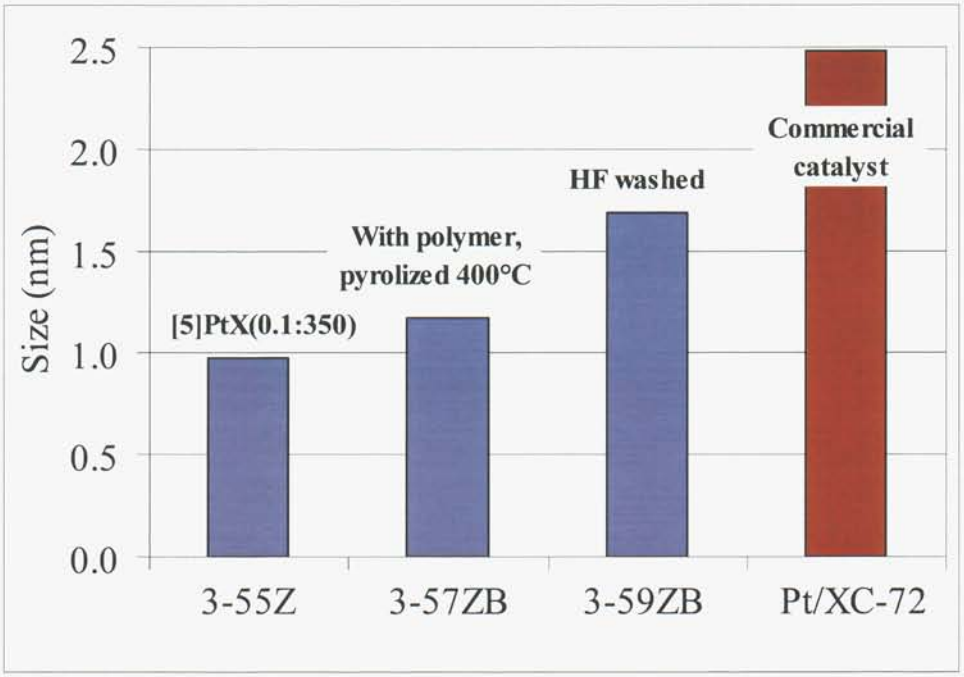

Figure 14. Calculated cluster sizes for one particular sample at various stages of catalyst synthesis, based on Pt-Pt coordination numbers from EXAFS analysis, using calculations of Ref. 19. The commercial electrocatalyst 20% Pt/XC-72 carbon from ETEK is shown for comparison.

The catalysts were also characterized by EDS during TEM investigation, and in most cases no residual Si, Al or Na could be detected, suggesting that all zeolite was removed during the acid treatment. Only for the highest Pt-loaded samples 2-54A and 2-54B was any residual silicon detected by EDS, and there the signals were very small relative to those of carbon and platinum, confirming only trace contamination.

1.7. Physical characterization of Pt/C electrocatalysts

The Pt clusters in the final electrocatalysts were characterized for their size distribution by TEM, their mean Pt-Pt coordination number (hence mean size) by EXAFS, and effective Pt-surface area and accessibility to the fluid phase by H_2 chemisorption and CO-stripping voltammetry. Other physical properties of the catalysts were monitored using EDS (presence of contaminants, and trends in Pt-loading), TGA/DTA (Pt-loading), BET Surface Area

analysis (bulk surface area and pore volume), and XANES (Pt oxidation state). Data for a selected suite of samples is presented below.

Pt/C catalysts prepared with varying Pt loading

Figure 15 shows selected TEM images of the final Pt/C catalysts prepared with a systematic variation in Pt-loading. A general trend of decreasing cluster size with decreasing Pt-loading can be seen (all images presented at same magnification). The mean cluster sizes range from about 2.8 nm (sample 2-54A) to about 1.4 nm (sample 2-54I). It is of particular interest to see the zeolitic lattice fringes present in images of some catalysts pyrolyzed at 800°C in the presence of propylene (e.g., Figure 15E and G). These fringes are formed from carbon (EDS verified no zeolite phase was present), and indicate how well the carbon was able to penetrate into the Pt-zeolite during impregnation and subsequent propylene treatment. The observance of fringes depends on the orientation of the lattice planes relative to the electron beam in the TEM, thus are not seen in every image. This large scale fringing was not observed for the high Pt-loaded catalysts (samples 2-54A through D), presumably due to the larger degree of pore obstruction by the Pt clusters. Furthermore, islands of graphitic fringes are seen in some catalysts as shown in the high magnification image of sample 2-54A (Figure 16).

Results of TGA/DTA analysis are summarized in Table 4, and shown in Figure 17. The Pt loadings were calculated assuming that the catalysts were pure Pt/C, with no residual zeolite or other impurities (which is supported by EDS data). The carbon light-off temperature quoted is the temperature at which the oxidation of carbon began. The maximum of the oxidation exotherm was considered an unreliable indicator of light-off since the heat generated by oxidation often skewed the exothermic peak, resulting in an unrealistic "maximum" value.

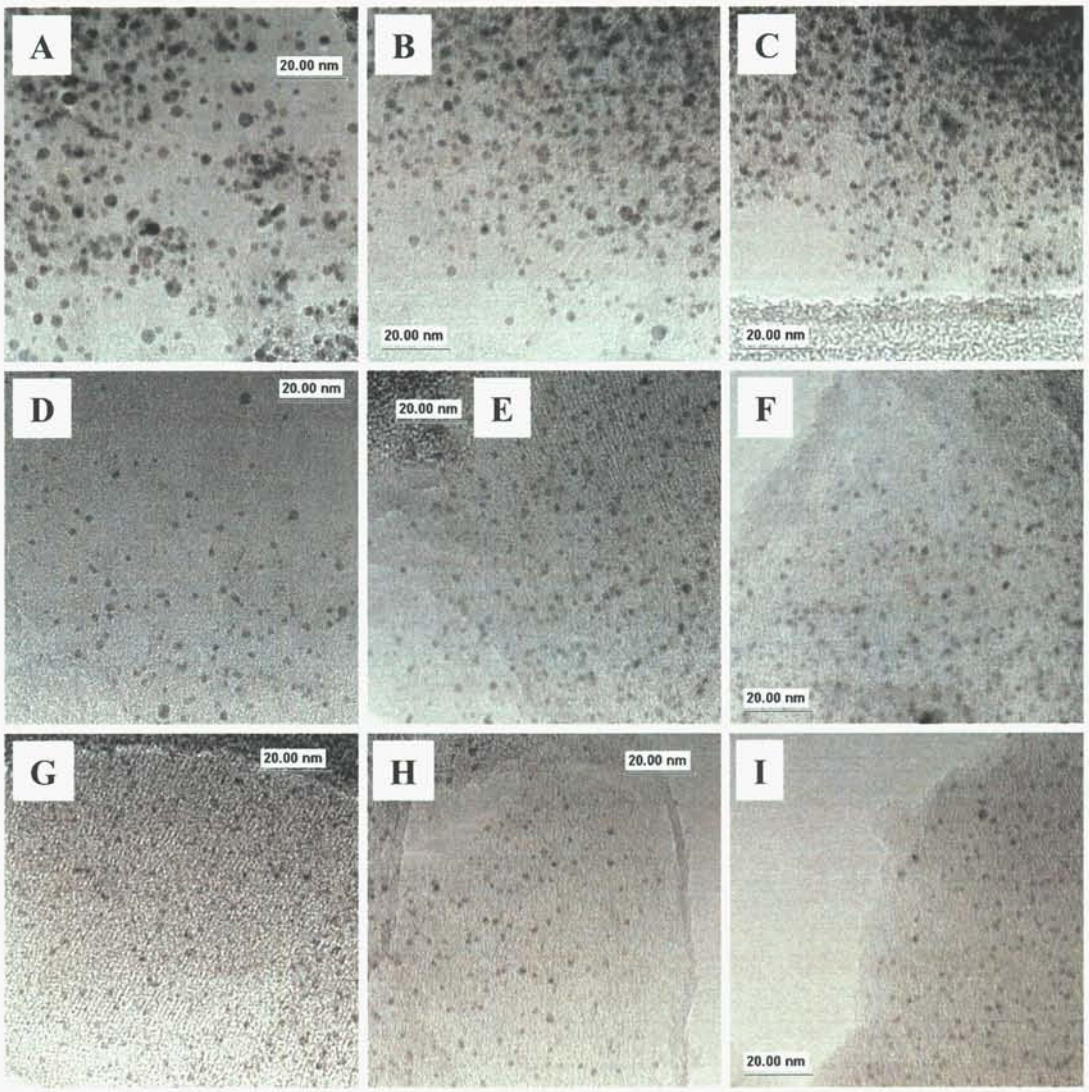

Figure 15. TEM images of Pt/C electrocatalysts possessing systematically varied Pt loadings. A: sample 2-54A, 47.7 wt.-%Pt/C from [20]Pt(0.1:350)/800/pp; B: sample 2-54B, 38.3 wt.-%Pt/C from [15]Pt(0.1:350)/800/pp; C: sample 2-54C, 20.5 wt.-%Pt/C from [10]Pt(0.1:350)/800/pp; D: sample 2-54D, 16.8 wt.-%Pt/C from [7.5]Pt(0.1:350)/800/pp; E: sample 2-54E, 12.2 wt.-%Pt/C from [5]Pt(0.1:350)/800/pp; F: sample 2-54F, 9.7 wt.-%Pt/C from [4]Pt(0.1:350)/800/pp; G: sample 2-54G, 7.8 wt.-%Pt/C from [3]Pt(0.1:350)/800/pp; H: sample 2-54H, 6.5 wt.-%Pt/C from [2]Pt(0.1:350)/800/pp; I: sample 2-54I, 3.6 wt.-%Pt/C from [1]Pt(0.1:350)/800/pp.

Table 4. Summary of data acquired by TGA/DTA on Pt/C electrocatalysts.

Sample	Pt-loading in Pt-zeolite[#] (wt.-%)	Limiting calcination ramp rate, n (°C min^{-1})	Carbon light-off* (°C)	Pt-loading in Pt/C (wt.-%)
2-54A	20.6%	0.1	350	47.7%
2-54B	13.9%	0.1	354	38.3%
2-54C	9.5%	0.1	378	20.5%
2-54D	7.0%	0.1	373	16.8%
2-54E	5.0%	0.1	392	12.2%
2-54F	3.9%	0.1	378	9.7%
2-54G	3.0%	0.1	374	7.8%
2-54H	2.0%	0.1	381	6.6%
2-54I	1.0%	0.1	378	3.6%
2-61A	9.5%	0.2	355	21.2%
2-61B	9.5%	0.3	372	25.9%
2-61C	9.5%	0.5	358	28.4%
2-61D	9.5%	1.0	360	22.7%
2-61E	9.5%	2.0	384	29.1%
2-61F	9.5%	5.0	396	29.3%

Pt-loading in zeolite determined via elemental analysis (AAS).
* Carbon light-off temperature defined as on-set of exothermic reaction seen in DTA.

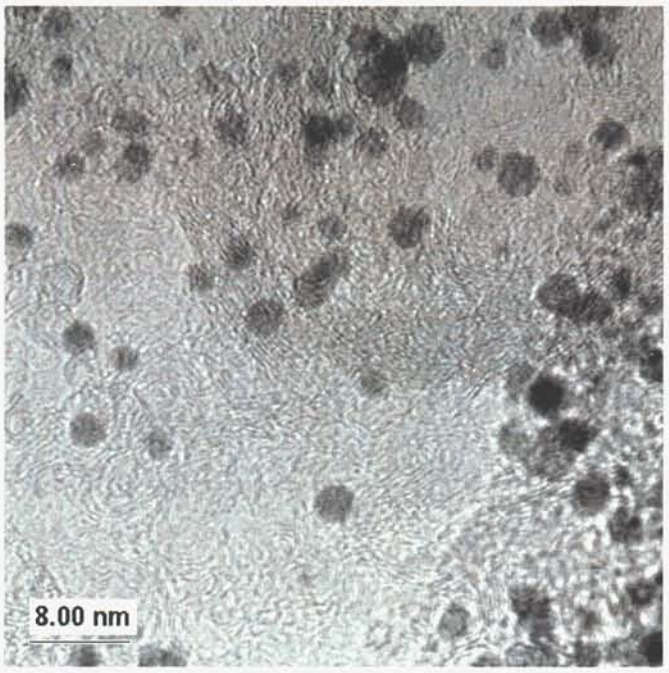

Figure 16. High magnification TEM image of sample 2-54A showing a large number of separate domains of lattice fringes for graphitic carbon.

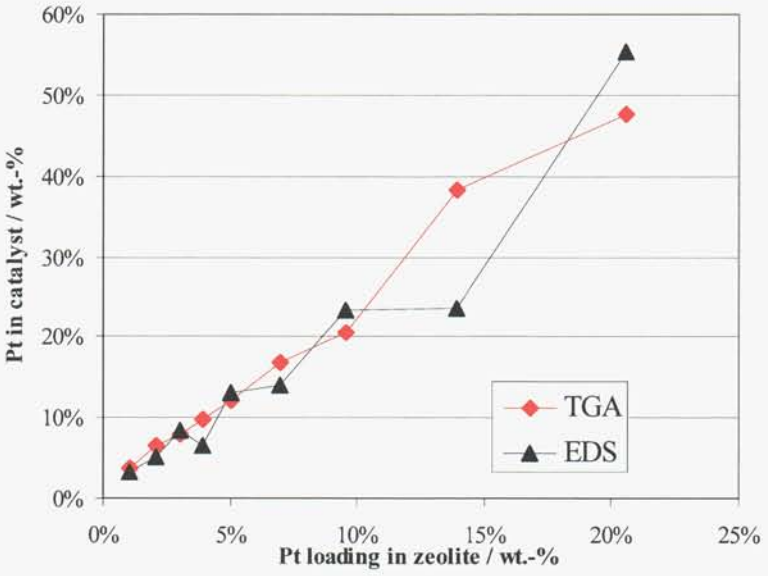

Figure 17. Pt-loading as derived from weight loss on burning out carbon in TGA/DTA as a function of loading of Pt in the original zeolite host. Data from EDS measurements is included to demonstrate that individual particles (as measured by EDS) follow same trend as bulk sample (as measured by TGA), confirming homogeneity of sample. Note, EDS data is not calibrated, and shows only trends.

Analysis of catalyst structure and cluster size by XRD was performed for sample 2-54H ([2]Pt(0.1:350)/C/800/pp), and revealed an average Pt cluster size, based on peak broadening, of 1.4 nm. In addition, a scan starting at low angle (Figure 18) picked up a broad hump representing a d-spacing of ~12.9 nm, arising from the observed regularity of the carbon's porous structure seen in the TEM images in Figure 15E and G.

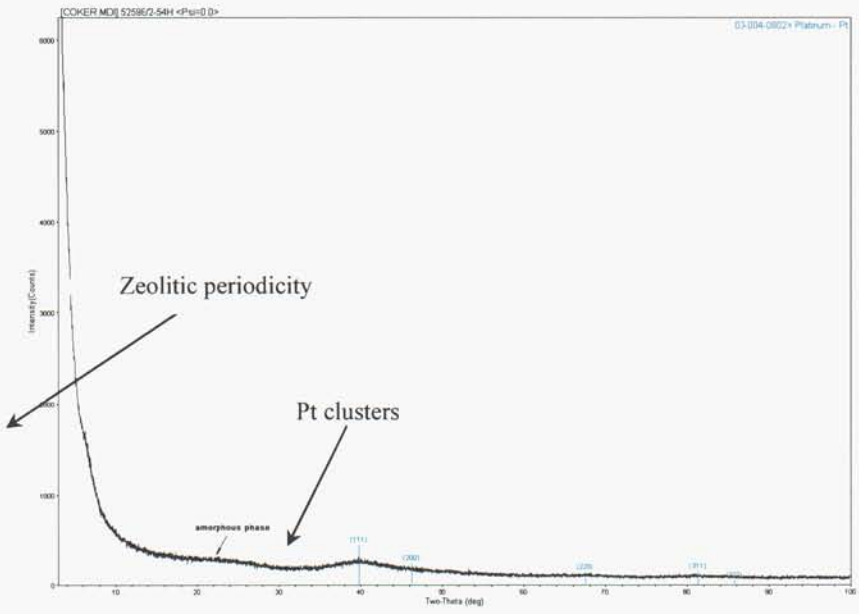

Figure 18. Low-angle X-ray Diffraction pattern of sample 2-54H. The broad humps indicative of Pt clusters, and of zeolitic structure in the carbon are indicated by arrows.

Pt/C catalysts prepared with varying calcination ramp rate

A second series of samples was prepared with nominally the same Pt loading (starting from 10wt.-% Pt in zeolite X), but with systematically varied calcination ramp rates (n) between 0.2 and 5 °C min^{-1}. Figure 19 shows selected TEM images of these catalysts, and a general trend of increasing Pt cluster size with increasing ramp rate may be recognized. A possible exception is sample 2-61E (n = 2.0 °C min^{-1}), which appears to possess larger Pt clusters than sample 2-61F (n = 5.0 °C min^{-1}). Sample 2-54C described above (derived from [10]Pt(0.1:350)/800/pp) may be considered one end-member of this series, with n = 0.1 °C min^{-1}.

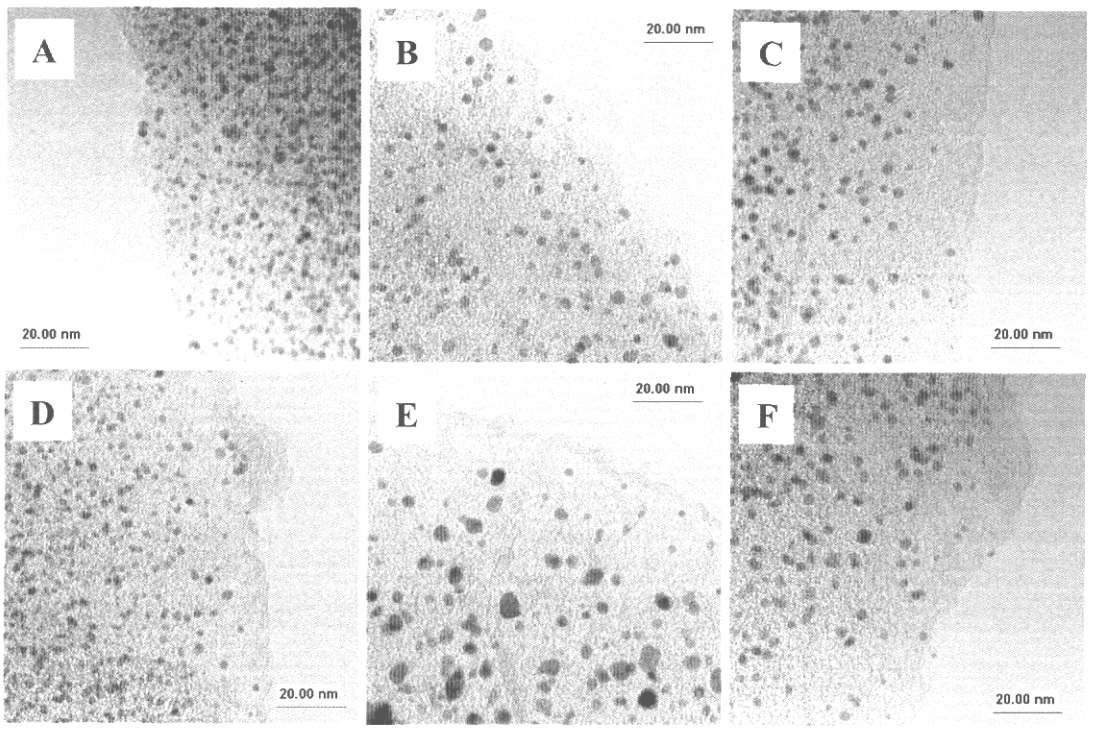

Figure 19. TEM images of Pt/C electrocatalysts possessing nominally the same Pt loadings, but calcined at different ramp rates (n). A: sample 61A, 21.2 wt.-%Pt/C from [10]Pt(0.2:350)/800/pp; B: sample 61B, 25.9 wt.-%Pt/C from [10]Pt(0.3:350)/800/pp; C: sample 61C, 28.4 wt.-%Pt/C from [10]Pt(0.5:350)/800/pp; D: sample 61D, 22.7 wt.-%Pt/C from [10]Pt(1.0:350)/800/pp; E: sample 61E, 29.1 wt.-%Pt/C from [10]Pt(2.0:350)/800/pp; F: sample 61F, 29.3 wt.-%Pt/C from [10]Pt(5.0:350)/800/pp.

Results of TGA/DTA analysis are summarized in Table 4 and Figure 20. The Pt loadings were calculated assuming that the catalysts were pure Pt/C, with no residual zeolite or other impurities (which is supported by EDS data).

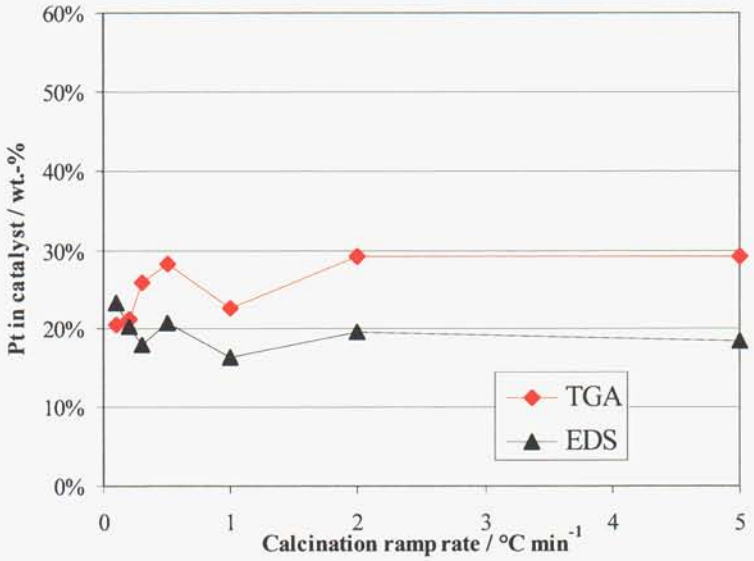

Figure 20. Pt-loading as derived from weight loss on burning out carbon in TGA/DTA as a function of calcination ramp rate (n). Data from EDS measurements is included to demonstrate that individual particles (as measured by EDS) follow same trend as bulk sample (as measured by TGA), confirming homogeneity of sample. Note, EDS data is not calibrated, and shows only trends.

1.8. Summary

Small, well-defined platinum clusters have been prepared in zeolite hosts through ion exchange and controlled calcination/reduction processes. Several factors influence cluster size, particularly the zeolite structure, Pt-loading and calcination protocol employed. Zeolite-supported platinum clusters below 1 nm and with narrow size distribution have been prepared and characterized. To enable electrochemical application, the pores of the Pt-zeolite were filled with electrically-conductive carbon via infiltratation with carbon precursors, polymerization/cross-linking, and pyrolysis under inert conditions. A series of carbon precursors, and methods of pyrolysis, was investigated, with conductivity of the resultant carbon as the metric. Low-temperature pyrolysis of infiltrated furfuryl alcohol, followed by in-situ decomposition of propylene at 800 °C was chosen as the preferred method. While greater electrical conductivity is achievable at pyrolysis temperatures of ~ 1000 °C, Pt cluster sintering and collapse of porous structure result in an overall decrease in catalyst performance with such high-temperature pyrolysis. The presence of the carbonaceous matrix has been demonstrated to mitigate Pt cluster sintering on thermal treatment, with ramifications for fuel cells of enhanced durability. The zeolite host was removed by acid washing, to leave a Pt/C electrocatalyst possessing quasi-zeolitic porosity and Pt clusters of well-controlled size. Pt cluster sizes in the final electrocatalyst ranged from ~ 1.4 nm to ~ 5 nm, depending on the Pt loading, calcination protocol, and pyrolysis conditions employed. For Pt/C catalysts prepared under optimal conditions, characterization by TEM revealed narrow cluster size distributions, islands of lattice fringes for graphite (required for high electrical conductivity) and, in some cases, a regular microporous structure within the carbon (templated by the zeolite host).

2. ELECTROCHEMICAL TESTS ON NANOSTRUCTURE PT/C POWDERS

2.1. Introduction

Pt/C electrocatalysts were synthesized with size controlled clusters for increased dispersion and to (potentially) take advantage of size effects as described in the previous section. Techniques such as TEM and XRD can characterize many important material characteristics, but to truly test the electrocatalytic viability of these materials, electrochemical experiments were performed. First, experiments were conducted to probe the electroactive surface area of the Pt clusters. Electroactive surface area is, by definition, Pt atoms available for chemistry. Pt atoms buried within the carbon matrix or within a Pt cluster are not counted. The theoretical surface area found by measuring average cluster size (using XRD for example), assuming all spherical particles, and extrapolating surface area based on Pt loading will never be realized because of occluded Pt clusters, Pt clusters not attached to the carbon matrix, etc. Aside from measuring the electroactive surface area, the kinetics of the oxygen reduction reaction was probed. The reduction of oxygen is the most difficult reaction within a fuel cell and needs the most active catalyst, so it is a very useful tool for studying electrocatalyst behavior. It is important to evaluate the electrocatalysts' performance in both ½ cell tests (more fundamental performance) as well as in fuel cell tests (long term performance); both of these experiments were performed and are described in the following section.

2.2. Experimental

Electrochemical experiments were performed using thin film voltammetric techniques of Schmidt, et al.(32) Electrodes were prepared by first making aqueous slurries of the nano-structured Pt/C powders as well as a standard Pt/C (ETEK, C1-20 20wt% Pt on Vulcan XC-72) in concentrations between 0.2 and $0.8\mu g_{Pt}/\mu l$. Multiple slurries were prepared to estimate uncertainty. Glassy carbon electrodes (GCE) 3 mm in diameter (area = $0.0707cm^2$) were polished with 0.05 μm Bio-Analytical Systems (BAS) alumina paste and sonicated in methanol prior to deposition of the catalyst powders. The aqueous slurries were sonicated for a minimum of 15 minutes; 5 μl of the slurry was deposited onto the cleaned GCE. The catalyst was allowed to dry before a thin coating (~0.5μm) of Nafion was applied (Aldrich Nafion 1100, 5 wt% in methanol further diluted 1:10 in methanol). The resulting catalyst loadings were between 1 and $4\mu g_{Pt}$, or between 14 and $57\mu g_{Pt}/cm^2$.

A standard three electrode cell was employed with a saturated calomel electrode (SCE) as the reference electrode, Pt wire as the counter electrode, and the catalyst coated GCE as the working electrode (WE). All potentials will be referenced versus the reversible hydrogen electrode (RHE). A BAS 100B potentiostat and a 628-10 Metrohm rotating disk assembly were used for the CO stripping and oxygen reduction reaction (ORR) experiments. Prior to all voltammetric experiments, each catalyst was electrochemically conditioned by briefly (5-10 sec) polarizing the WE to potentials where hydrogen adsorption and evolution occur (*i.e.*, $<0mV_{RHE}$). After evolved H_2 was removed from the WE, CO was adsorbed onto the electrocatalyst surface by holding the potential at $100mV_{RHE}$ for 3 minutes in a 0.5M H_2SO_4 solution (sulfuric acid was diluted with de-ionized water from Fisher Scientific 36N reagent A.C.S. grade H_2SO_4) saturated with ultra high purity (UHP) CO. This was done while rotating the WE at 1000rpm to increase mass transfer. The potential was then swept at 20mV/s from 100 to $1265mV_{RHE}$. (*N.B.* Background voltammograms were performed on carbon support only to ensure carbon does not adsorb CO.)

For the ORR experiments, the electrocatalyst surface was first electrochemically conditioned and evolved H_2 was removed as described above. The potential was swept from 1265 to 165mV$_{RHE}$ at 5mV/s while the WE was rotated at 500, 1000, 1500, 2000, and 2500rpm in a UHP O_2 saturated 0.5M H_2SO_4 solution. For the ORR experiments, different electrodes of various loadings were again tested for each electrocatalyst. Both CO stripping and ORR experiments were performed at laboratory temperature, 20-22°C.

Two fuel tests were also performed for a side-by-side comparison of a Pt/C material versus the ETEK 20 wt% Pt on Vulcan XC72 carbon. The Pt/C material was calcined at the 0.1°C/min ramp rate, the pyrolysis temperature was 900°C, and the final Pt wt% was 23%. The anode electrode assembly in each test was fabricated from 1) Nafion 1100 5 wt% in alcohol, and 2) Pt Black as an inked dispersion onto a Nafion 117 (7 mil thick) membrane. The anode electrode assembly had a loading of 5mg$_{Pt}$/cm^2 and a Nafion content of 10 wt%. The cathode featured either the Pt/C catalyst or the ETEK material; each cathode assembly was prepared in the same way as the anode with equivalent loadings of 1.5mg$_{Pt}$/cm^2 and a Nafion content of 30 wt%. Once the electrodes were cast onto the membrane and dried, they were put into two separate fuel cell rigs (*i.e.*, rig #1: anode is Pt Black, cathode is ETEK material; rig #2: anode is Pt Black, cathode is Pt/C material). For both cases, a toray paper/microporous layer was used as the backing for the electrodes. The cells were conditioned for 24 hours at 80°C with a 20sccm H_2 flow to the anode and a 20sccm O_2 flow to the cathode. A potentiostatic lifetime test was then performed for 300 hours (12.5 days). The potential was held at 0.5V and 80°C while the flow rates were reduced to 2sccm on both the anode and cathode side.

2.3. Results and Discussion

Figure 21 shows a typical CO stripping voltammogram for a 47.7 Pt wt% Pt/C sample (d-54A) (0.1°C/min ramp rate). The peak at 925mV$_{RHE}$ is from current being passed as CO adsorbed on the electroactive Pt surface (Pt-CO) is stripped (or, oxidized) according to the following reaction:

$$Pt\text{-}CO + H_2O \rightarrow CO_2 + 2H^+ + 2e^-$$

The exact shape and position of the stripping event changes but for our purposes is not important. The important parameter is the charge (Q) resulting from the CO oxidation event,

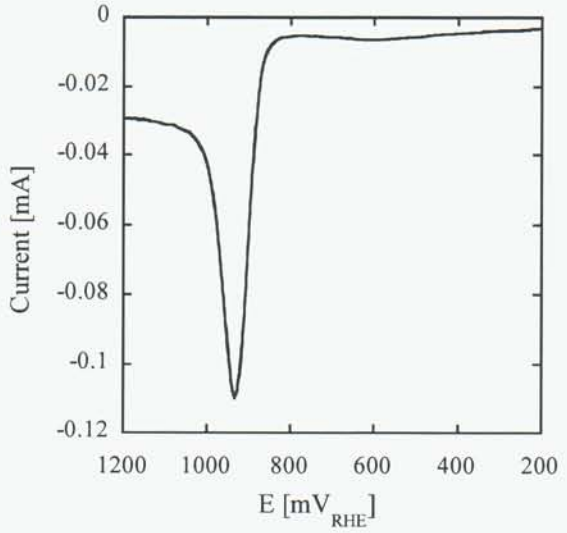

Figure 21. Current versus potential for a 47.7 wt% Pt sample (2-54A) carbonized at 0.1°C/min. The peak represents current associated with the oxidation of CO to CO_2 and can be related to electroactive Pt surface area.

which is calculated by integrating the current as a function of time. Q can then be related to the electroactive surface area of Pt by first plotting Q versus the Pt loading on the electrode surface (Figure 22). The data is then regressed to a straight line with an intercept through zero and the electroactive surface area of Pt ($SA_{eactive}$) can be calculated as follows:

$$SA_{eactive} = 1{,}000 * Slope * N_A/F * XSA_{Pt}/n$$

where Slope [=] $mC/\mu g_{Pt}$, N_A = Avogadro's number (6.022×10^{23} atoms/mol), F = Faradays constant (96,486 C/mol e^-), XSA_{Pt} = atomic cross-sectional area of a Pt atom (8.00×10^{-20} m^2/atom), n = number of electrons in CO oxidation reaction ($2e^-$), and 1,000 is a metric conversion factor. This particular sample yielded a surface area of 111.6 +/- 12.0 m^2/g_{Pt}, which

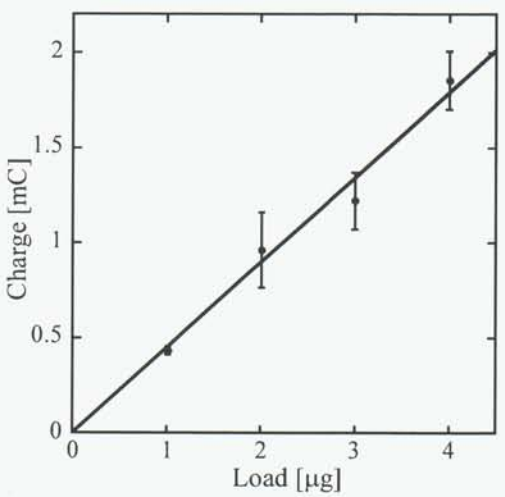

Figure 22. Charge versus load from CO stripping experiments for the same sample shown in Figure 21. The electroactive surface area is calculated from the slope of the best fit line (0.45mC/µg). The resulting surface area is 111.6 +/- 12.0 m^2/g_{Pt}.

compares very favorably with the ETEK 20 wt% Pt material (86 m^2/g_{Pt}), especially when one considers that surface area typically decreases with increased Pt loading.

Electroactive Pt surface area data from several series of samples were acquired and analyzed. The first series held all synthesis variables constant except Pt loading, which was varied from 3.6 to 47.7 wt% (calcination temperature ramp rate = 0.1°C/min, pyrolysis temperature = 800°C). Following the methodology presented in Figure 21 and Figure 22, the surface area values were calculated and are presented in Table 5 along with the Pt wt%. A correlation between Pt wt% and surface area was expected, with increasing Pt wt% resulting in a decrease in surface area. The logic behind this is as Pt wt% increases, the probability that Pt nanoparticles will combine, sinter, and form larger particles increases and, as a result, the surface

Table 5. Electroactive surface area compared to Pt wt%.

Sample	Pt Wt % in electrocatylist	Electroactive Surface Area (m^2/g_{Pt})
2-54A	47.7	111.6 +/- 12.0
2-54B	38.3	64.4 +/- 6.1
C	20.5	93.0 +/- 10.8
D	16.8	83.2 +/- 12.6
E	12.2	81.7 +/- 3.4
F	9.7	103.8 +/- 18.7
G	7.8	102.9 +/- 5.2
H	6.6	69.3 +/- 5.1
I	3.6	38.3 +/- 8.4

area decreases. In fact, ETEK notes that their 20 wt% Pt sample has 2.5nm particles while their 40 wt% Pt electrocatalyst has 3.9nm particles. This trend is not seen in the series of samples presented in Table 5. The reason for this is likely variability when impregnating with the carbon precursor which in some cases likely leads to more Pt particles being occluded. This effect is likely exacerbated when the Pt load decreases.

A second series of samples was tested for electroactive surface area, this time the Pt wt% and pyrolysis temperature were held constant at 800°C and *ca.* 20%, but the calcination temperature ramp rate was varied from 0.1 to 5°C/min. These results are presented in Figure 23. Since particle size is strongly influenced by the calcination temperature ramp rate, one would expect the surface area to increase as the ramp rate is slowed. In this case, the data follows the expected trend and a strong correlation is seen. It should be noted that the electroactive surface area for the 20 wt% samples with the slower ramp rates (0.1 and 0.2°C/min) compare well with the 20 wt% Pt sample from ETEK (86m^2/g_{Pt}).

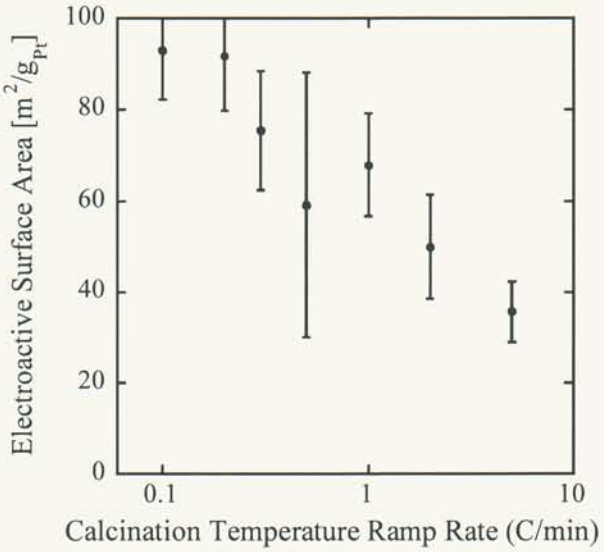

Figure 23. Pt surface area as calculated from CO stripping experiments as a function of calcination temperature ramp rate (a good indicator of particle size); as ramp rate increases area decreases.

The oxygen reduction reaction (ORR) was also investigated using a rotating disk electrode (RDE) assembly to probe electrocatalyst kinetics and, ideally, to see which of the following two reactions is occurring:

$$O_2 + 2H^+ + 2e^- <-> H_2O_2$$

$$O_2 + 4H^+ + 4e^- <-> 2H_2O$$

with the $4e^-$ reduction to H_2O being preferred. The reduction of oxygen is the most difficult and accounts for the most losses within a fuel cell; thus, increasing the efficiency of this reaction is one of the primary interests of the fuel cell community. Figure 24 shows RDE polarization curves for a 9.7 wt% Pt sample (2-54F) calcined at 0.1°C/min compared to the 20 wt% Pt ETEK standard. The potential was swept at 5mV/s in an O_2 saturated 0.5M H_2SO_4 solution while the RDE was rotating at 2000rpm. The theoretical onset potential (*i.e.*, the potential at which the current begins to increase, indicative of oxygen reduction) for the ORR is $1.2V_{RHE}$, but because of losses this is never achieved (it is typically ~$0.85V_{RHE}$). Note how favorably the onset potential for the Pt/C catalyst compares with the ETEK material. As the potential continues to decrease towards

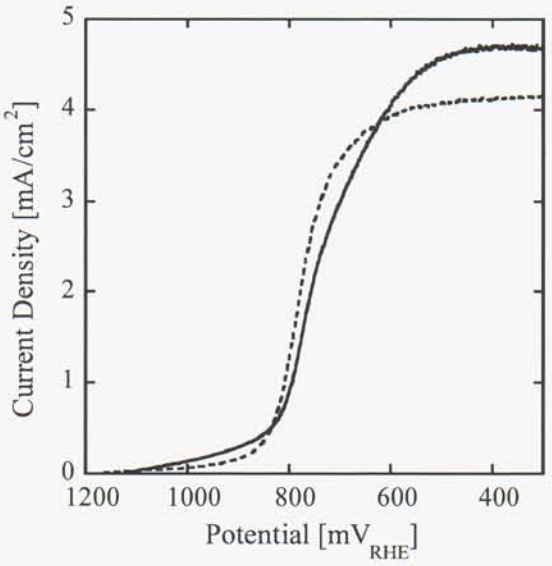

Figure 24. Oxygen reduction polarization curves for a 20 wt% Pt ETEK material (- - -, 4.1μg_{Pt}) and a 9.7 wt% Pt sample (2-54F) (-, 4.5 μg_{Pt}). cm^2 is the geometric area of the electrode.

400V_{RHE}, the current increase until a plateau is reached (the mass transfer limited current, i_{lim}). The behavior seen in Figure 24 is expressed mathematically as follows:

$$1/i = 1/i_{kin} + 1/i_{lim} + 1/i_{film}$$

where i = total current, i_{kin} = kinetically limited current and i_{film} is the film diffusion limited current.(32, 33) i_{film} is present in analyses of porous electrocatalysts, such as the Pt/C materials discussed here, because of the additional resistances of the Nafion layer and the microporous carbon matrix. If the experiments were performed with a perfectly planar electrode (i.e., zero porosity) and with a Nafion thickness approaching zero, the term $1/i_{film}$ becomes negligible and the equation simplifies to:

$$1/i = 1/i_{kin} + 1/i_{lim}$$

In this case, a traditional Levich analysis can be performed by acquiring RDE data at multiple rotation speeds and plotting $1/i_{lim}$ vs $1/\omega^{1/2}$. i_{lim} is defined as follows

$$i_{lim} = [0.62nFACD^{2/3}\nu^{-1/6}]\omega^{1/2}$$

where F is again Faradays constant, A is the electrode surface area (0.0707 cm^2), n is the number of electrons participating the reaction, C = O_2 solubility in 0.5M H_2SO_4 (typical value is 1.22x10^{-6} mol/cm^3)(34), D = diffusion coefficient of O_2 through 0.5M H_2SO_4 (typical value is 1.04x10^{-5} cm^2/s)(34), and ν = kinematic viscosity (typical value is 9.87x10^{-3} cm^2/s)(35). In a traditional Levich analysis ($1/i_{lim}$ vs $1/\omega^{1/2}$), the intercept ($1/i_{kin}$) goes to zero and the slope becomes

$$\text{Slope} = [0.62nFACD^{2/3}\nu^{-1/6}]^{-1}$$

n can now be easily calculated and the predominant ORR determined. Polarization curves at multiple rotation speeds for the 9.7 wt% Pt sample first shown in Figure 24 are presented in Figure 25a; the corresponding Levich plot is shown in Figure 25b.

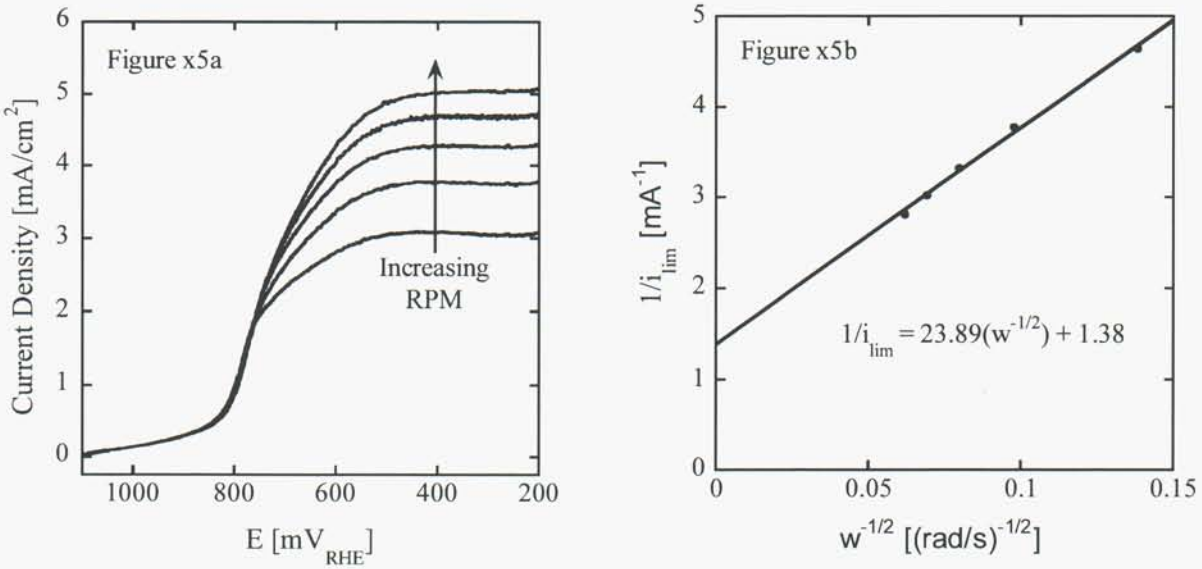

Figure 25. The left plot shows ORR polarization curves for a 9.7 wt% Pt/C sample (2-54F) at 500, 1000, 1500, 2000 and 2500rpm. The right plot shows a Levich plot of the data from the left plot. Note the lack of a zero intercept, though the regression fit is very accurate ($R^2 = 0.996$).

Unfortunately, as alluded to above, the resistance of the Nafion film and the resistance of O_2 through the microporous carbon layer negates acquiring a value of n from the Levich plot (*i.e.*, assuming $1/i_{film}$ is negligible is not valid). This point is made more clear by examining the definition of i_{film}:

$$i_{film} = nFAD_f c_f/\delta_f$$

where D_f is the diffusion of O_2 through the Nafion/carbon film, c_f is the O_2 concentration in the Nafion/carbon film, and δ_f is the Nafion/carbon film thickness.(36) Since i_{film} depends on n and contributes to the total current (i) in all regions of the polarization curve, i_{kin} and i_{lim} cannot be isolated and n cannot be calculated using a Levich analysis. If the diffusion/concentration of oxygen through/in the carbon matrix could be determined from independent experiments, one could perform a modified Levich analysis.(37) This is not trivial, especially for samples with a varying carbon matrix. Thus, quantitative values cannot be acquired from the ORR data, but qualitatively the Pt/C materials can be compared to the ETEK materials as is done in Figure 24. This qualitative comparison confirms electrocatalytic performance comparable to commercially available electrocatalysts. (*N.B.* Having ORR polarization curves approaching the performance of the ETEK material is a common result for the materials synthesized here, for additional ORR results of the series of samples with varying calcination temperature ramp rates and varying Pt wt%, please refer to Appendix B.)

In an effort to quantify the performance of these materials and to understand their long term behavior, a side-by-side fuel cell test was completed to compare the performance of a Pt/C material (3-85d) versus the ETEK 20 wt% Pt on XC72 electrocatalyst. The membrane electrode assemblies (MEA) were prepared in the exact same manner except one MEA's cathode electrocatalyst was a Pt/C material (0.1°C/min, pyrolysis temperature was 900°C, 23 wt% Pt) while the other MEA utilized the ETEK material. A 300 hour potentiostatic test was performed at 0.5V. The results of this test are shown in Figure 26; the Pt/C material's results are in red and

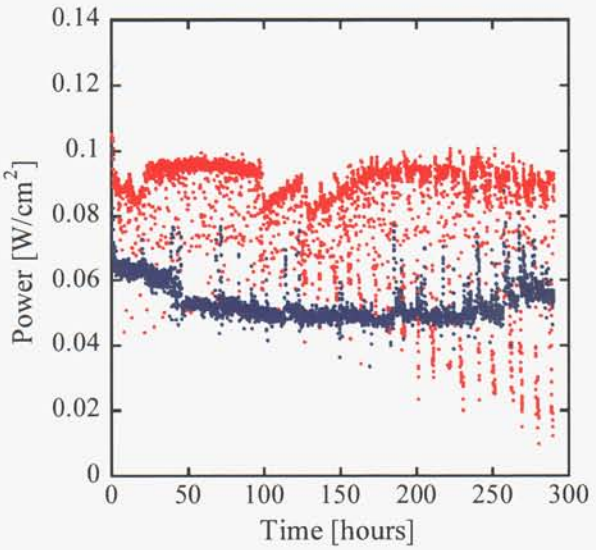

Figure 26. Two fuel cell tests comparing a 23 wt% Pt/C material (sample 3-85d) (red) versus the ETEK 20 wt% Pt (blue). Each test had a similarly prepared anode ($5mg_{Pt}/cm^2$) and differed only in the cathode; either Pt/C or ETEK.

the ETEK material's results are in blue. The Pt/C material has an *average of 50% greater power* than the ETEK material. The noise in the data, especially from the Pt/C test, is due to classic water management issues at the cathode. These issues can typically be engineered out of the system by optimizing the MEA for a specific electrocatalyst. This was not done for the Pt/C material; doing so would decrease the amount of noise in the data as well as likely improve average performance. The most encouraging piece of information from this fuel cell experiment is that Pt/C performed better than the ETEK material and it performed well over time, supporting speculation that these Pt/C materials help resist sintering and may have enhanced long-term stability compared to what is currently available.

2.4. Summary

These Pt/C materials had as much as 110 m^2/g_{Pt} electroactive surface area, an almost *30% improvement* over what is commercially available (86 m^2/g_{Pt}). These Pt/C materials also perform qualitatively as well as the ETEK material for the ORR, a non-trivial achievement. The fuel cell test showed that Pt/C outperformed the ETEK material by an *average of 50%* for a 300 hour test. Increasing surface area decreases the amount of Pt needed in a fuel cell, which translates into cost savings. Furthermore, the increased performance realized in the fuel cell test might ultimately mean less Pt is needed in a fuel cell; this again translates into cost savings. Finally, enhanced long-term stability is a key driver within the fuel cell community as improvements in this area must be realized before fuel cells find their way into the marketplace; these Pt/C materials hold great promise of enhanced stability over time.

3. LASER DESORPTION/IONIZATION MASS SPECTROMETRY

This section will focus on the instrument setup, experimental operating conditions, and then results obtained from the new laser ablation ion source.

3.1. New Laser Desorption Ion Source for FT-ICR Mass Spectrometry

The existing FT-ICR mass spectrometer has a 3.3 Tesla superconducting magnetic, a dual cubic trapping cell connected by a 0.030-in. conductance limit (38), and is controlled by the MIDAS software from the National High Magnetic Field Laboratory (39). The existing system is shown configured with the new laser desorption/ionization (LDI) components in Figure 27.

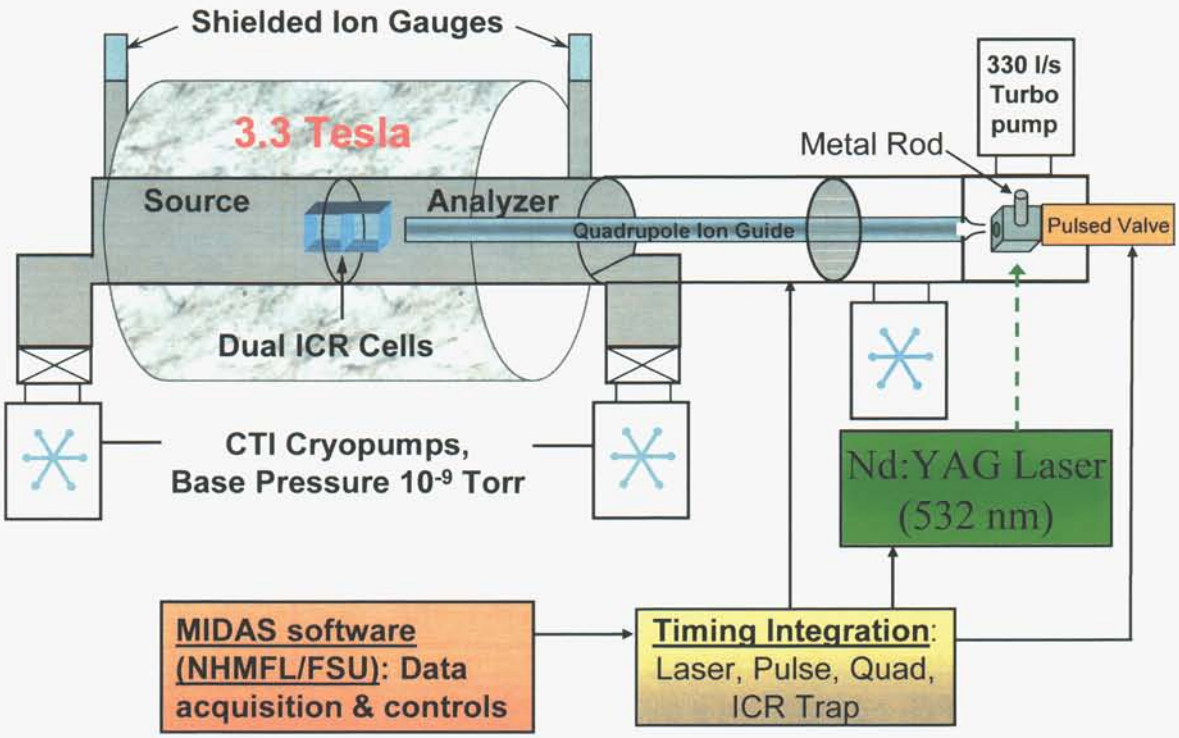

Figure 27. Existing FT-ICR mass spectrometer (top left) with new LDI components.

Several instruments were required to make the external laser ablation ion source and couple it to the existing mass spectrometer. These new primary components are: A Continuum Surelite Nd:YAG laser, purchased with capital equipment funds; a fast pulsed source (R. Jordan, duration ~40 μs); a quadrupole ion guide (IonSpec). Individual settings for these components are discussed here.

The Nd:YAG laser was operating with the doubled 532 nm (visible green) output known to be an excellent wavelength range for metal desorption and ionization (40-43). Of note, platinum clusters have been generated by using the fundamental 1064 nm output (44). This laser can flash (and fire) by internal timing or external triggering.

The pulsed valve controller also has internal or external triggering function. Only the external triggering is of interest for this application. The external triggering has a built-in variable

delay (course screw and fine knob adjustment), which it turns out is critical to variably synchronize with the laser output (either before or after the laser pulse).

Operation of the IonSpec quadrupole is not intended to be continuous, both because the electronics are not designed for continuous-wave operation and the electric field seen at the ICR cell detection plates is quite significant. Ideally, a pulse into the "gain" input on the high voltage/high frequency generator will turn on and run this quadrupole only during the time necessary to transmit ions through to the ICR cell for trapping.

3.2. Operating Conditions for LDI/FT-ICR Mass Spectrometer

Successful operation of this new instrument configuration depended mostly upon the proper synchronization of timing signals. It was thought that the "single shot" feature on the laser could be utilized; this would have allowed internal 10 Hz flashlamp operation and then selection of the next flash to lase (Q-switch firing). However, the single shot input requires an intermittent short to emulated the manual pushbutton be made, and this was not readily replicated with simple electronics. With the FT-ICR controlling software, MIDAS, unable to accept trigger signals (hardware fault suspected), and the laser needing to run near 10 Hz continuously, unique external triggering with a decoupling from MIDAS was required. The schematic of the triggering and pulse signals is shown in Figure 28.

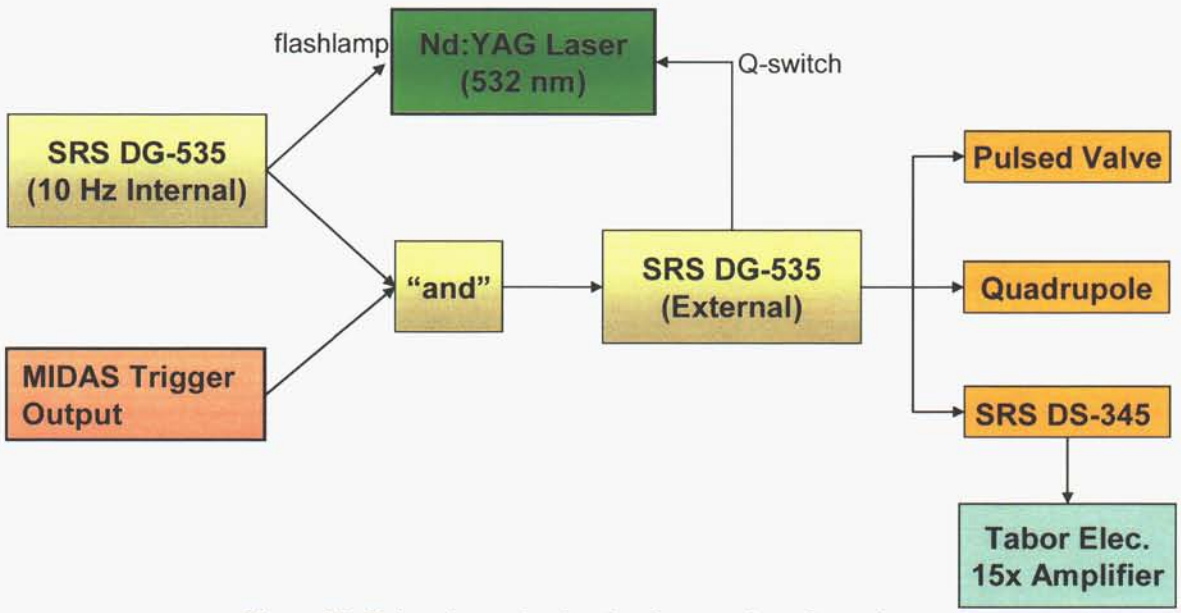

Figure 28. Triggering and pulse signal connection schematic.

The laser flashlamp is run continuously by the internally triggered 10 Hz output from a Stanford Research Systems (SRS) DG-535 delay/pulse generator (inverted TTL of 10 μs). A synchronous, but not inverted, output TTL is also sent to a simple "and" circuit. This "and" circuit will pass the flashlamp timing signal when a signal is also being sent from a MIDAS trigger; the MIDAS trigger is set for 100 ms width so as to capture one, and only one, of the 10 Hz flashlamp triggers. The output TTL from this "and" circuit then triggers a second DG-535 delay/pulse generator. This second DG-535 then has several outputs: the trigger output line (T_0) is sent right to the pulsed valve; a variable voltage pulse (AB) is sent to the "gain" input of the quadrupole to turn it on and off with the "A" delay time set to zero;

inverted TTL pulse (CD) fires the Q-switch on the laser (290–330 μs from T_0, 10 μs width); then the "B" trigger delay is set to the time at which one turns on the trapping voltages (triggering the waveform generator) and turns off the quadrupole ion guide (typically Q-switch delay plus 1 ms). The waveform generator is an SRS DS-345, and is set up to put out a sawtooth waveform going from ground to high when triggered, then decaying linearly back to zero volts; typical settings were amplitude of 1 V, offset of 0.5 V, phase equal to 180°, and frequency from 0.25–0.1 Hz (4 to 10 second decay). The DS-345 output is sent first through a 15x wideband amplifier (Tabor Electronics, model 9200) to generate a 15 V peak trapping pulse. Sometime during the decay of the output voltage from the DS-345 the MIDAS system, having waited a sufficient amount of time, sends an analogue output to set the minimum trapping voltage; this voltage needs to be increased by 0.6 V from the desired trapping voltage due to a diode voltage drop, see Figure 29 for the trapping voltage circuit connection.

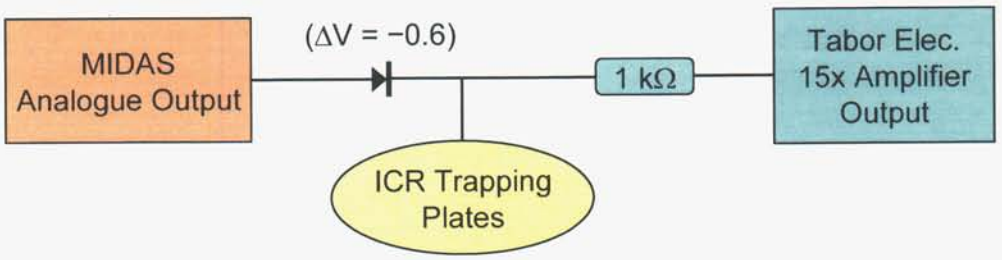

Figure 29. Simple circuit for trapping plate voltage control.

3.3. Results from LDI/FT-ICR Mass Spectrometer

Once assembly and alignments were completed and the triggering issues worked through, ion signals were monitored at the analyzer end and conductance plates in order to find when the LDI ion packet was arriving at the ICR cell. With the platinum rod in place, a signal was observed, after the laser shot, to rise at approximately 0.5 ms, peak at 1 ms, and decay by approximately 2 ms. Once this was seen, the quadrupole-off and trapping plate-on times were set to 1 ms from the laser shot.

Positively charged platinum atoms were then readily observed with a strong signal strength, but lack signs of any cluster formation, i.e. Pt^+_n with $n = 1$ only (Figure 30a). However, a high resolution spectra is obtainable, with over 100,000 mass resolution determined from FWHM at the platinum atom mass range (194–198) (Figure 30b). The very high mass resolution is due to the long transient signal acquired here for 0.82 seconds, and which could be increased by a factor of two or four as necessary. The small peaks next to the primary platinum signals represent various sidebands; these typically reflect both plus and minus magnetron and trapping frequencies. This particular spectrum used argon gas in the pulse nozzle, with the Q-switch delay on the laser set at 325 μs (flashlamp voltage at 1.25 kV)

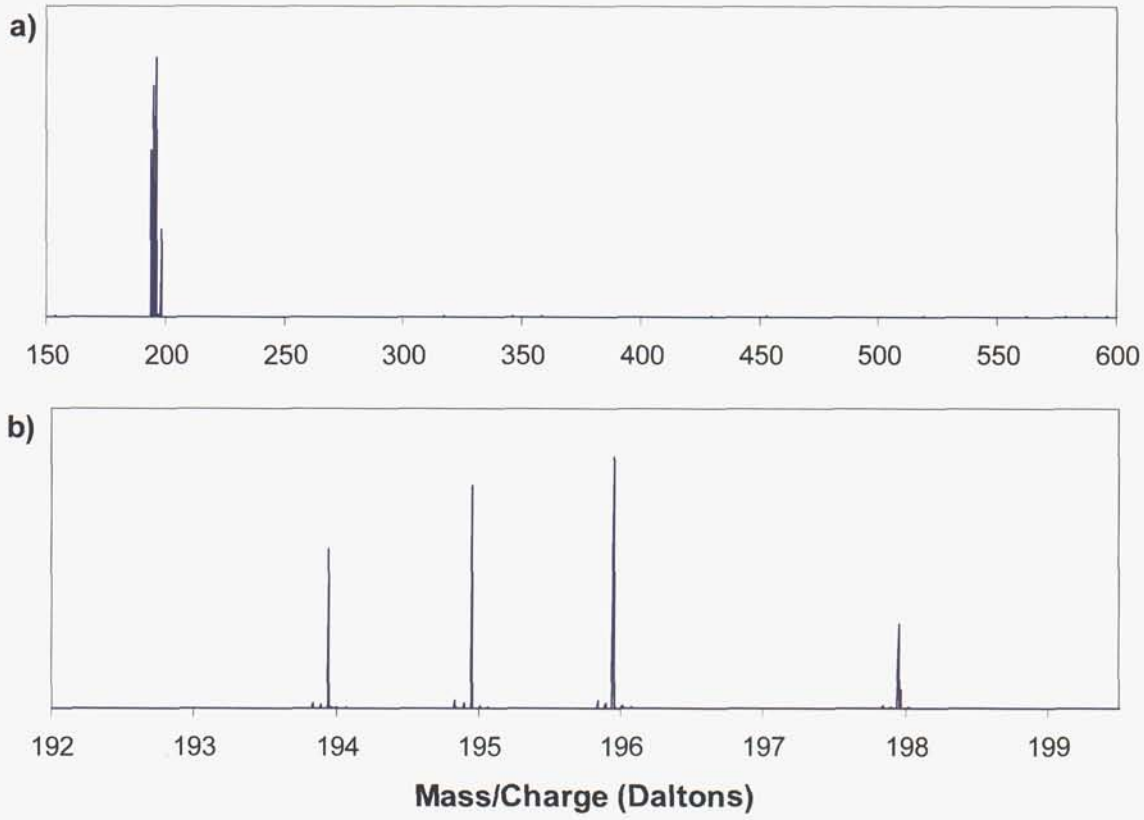

Figure 30. Resulting LDI platinum mass spectra: a) broad range; b) narrow range.

The lack of any cluster ion signals being observed then led to many attempts to modify the experimental conditions in order to generate clusters. For example:

- Switching the quadrupole operating frequency from 1.3 MHz to 800 kHz, which resulted in no observable ion transmission;
- scanning the pulse valve delay;
- raising and lowering the laser power.

Deciding that the clustering was not occurring within the source, the pulsed nozzle gas was changed to neon and then to helium. Helium is typically used within such sources as it appears to more efficiently cool and condense metal plasmas. However, it is not pumped well by the cryogenic pumps on the system (3 of the 4 primary pumps, see Figure 27). Even use of helium gas with backing pressures up to 8 atmospheres in the pulsed valve did not produce detectable clustering.

Further literature research seemed to indicate that the cluster source itself was not of an optimal geometrical configuration for generating clusters. In the haste for results, a new cluster source to couple the LDI metal plasma with the pulsed nozzle gas was machined. Teflon was chosen as the material due to the ease of machining and because an appropriately sized piece was available. The approximate dimensions of this source are drawn in Figure 31. The most important dimensions appear to be the initial chamber, or "waiting room" (as coined by Smalley's group in (45)), and then the further reaction and expansion zone. The previous

source had a rather large (~ 1/8 inch i.d.) initial chamber that quickly expanded further with a 10 degree opening.

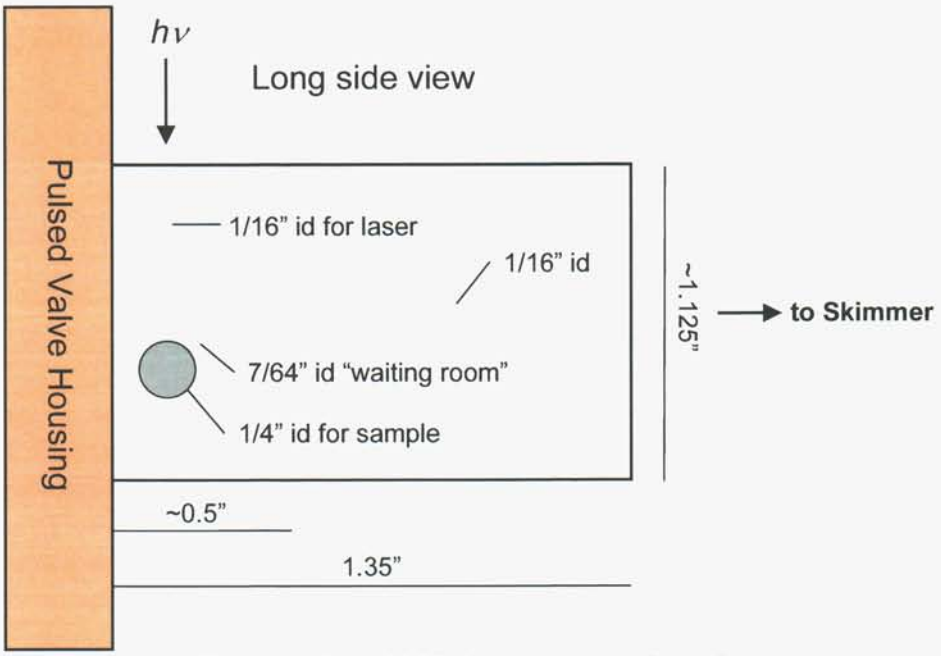

Figure 31. Second LDI cluster source configuration.

Using this new LDI source "chamber", clusters of platinum were still not observable.

To better characterize and optimize performance of this new source design several parameters were systematically varied and the platinum cation signal measured. Standard experimental conditions were 8 atmospheres helium pulsed nozzle backing gas pressure, skimmer at +1 Volts, quadrupole offset to −1 Volts, pulsed nozzle firing 14 μs before laser, the quadrupole at 1.3 MHz with 3.2 V gain pulse, trapping voltage delay at 1 ms, and a 5 second trapping plate voltage decay from 15 V peak. Five scans are collected and averaged for each data point.

Figure 32 shows the signal variation as a function of trapping time delay from the firing of the laser. A strong peak is exhibited at about 1 ms delay time, with a slower decay of the signal strength as the delay is increased to about 1.5 ms.

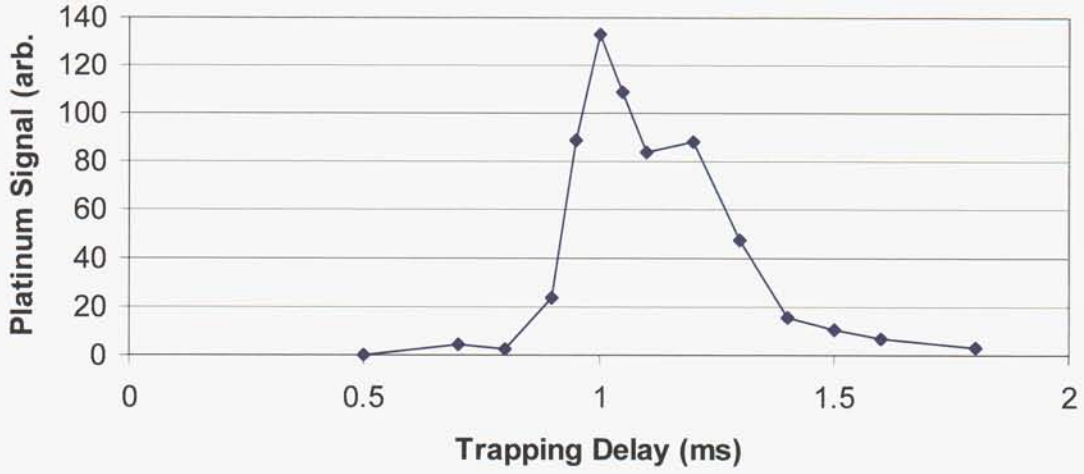

Figure 32. Signal level as a function of trapping time delay.

The quadrupole gain input line both varies the output strength of the quadrupole voltage as well as controls its on/off timing. The variation in ion transmission depends strongly upon this quadrupole voltage level. As shown in Figure 33, only when the gain inputs are between about 2.75 through 3.5 V (where quadrupole output is from about 175 to 250 $V_{peak\text{-}peak}$) for the 1.3 MHz output are platinum cations passed through.

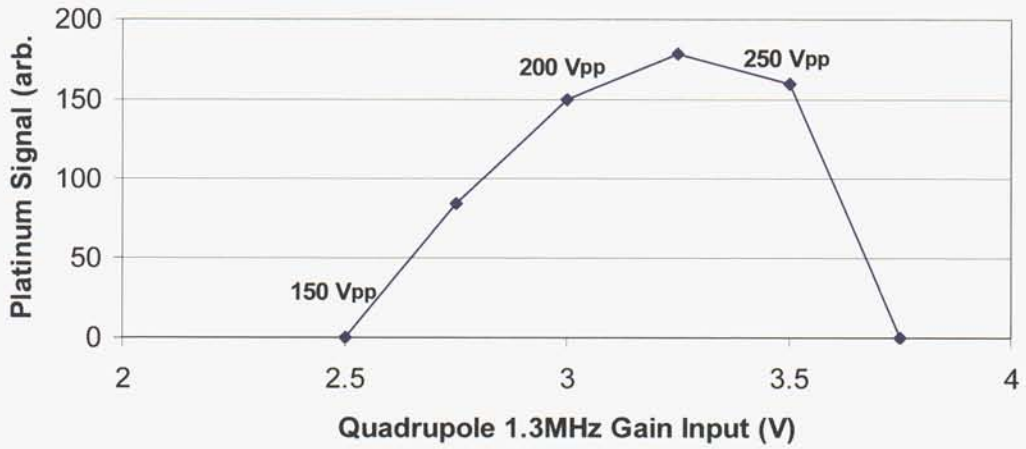

Figure 33. Signal level as a function of quadrupole gain.

Lastly, the variation in the platinum cation signal was examined as a function of the pulsed nozzle delay time relative to the desorption/ionization laser shot. It is noted that from the onset of the pulsed nozzle current to the actual opening and flow of gas from the valve is a delay on the order of tens of microseconds. It is seen by Figure 34, that if the pulsed nozzle opens very early that the ion signal decreases. Somehow the high background gas already in the "waiting room" interferes with ion entrainment to the skimmer. The level of signal without any gas pulse was measured to range from 113 to 139 from three determinations.

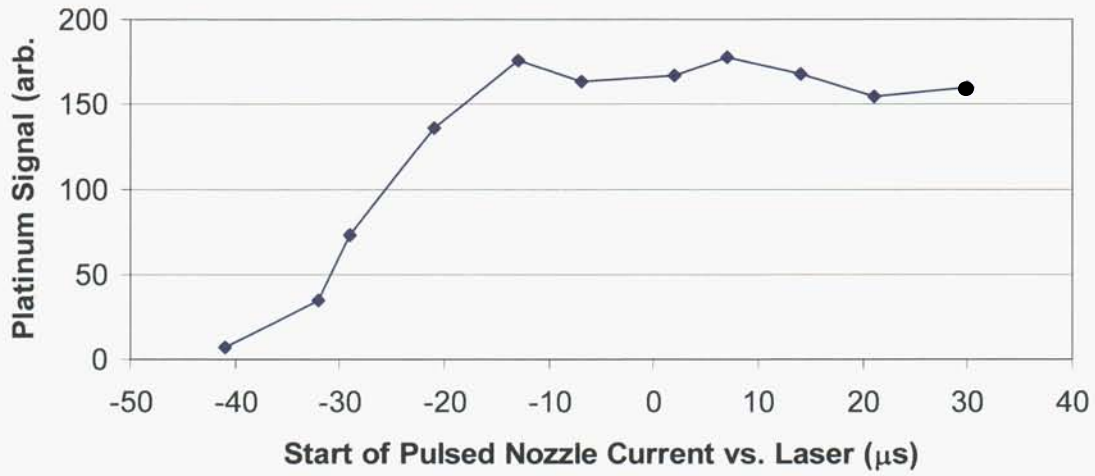

Figure 34. Signal level as a function of pulsed nozzle timing.

An alternate sample of copper, with cesium iodide on it, was tried in order to observe some type of clustering. No copper metal clusters or atoms were observed, however plenty of iodide signal, and two or more series of CF_2 clusters do exist. These Teflon fragment clusters range from about 300 to 800 Daltons, the spectra is shown as Figure 35. A particularly strong signal at 365 Da, with a potentially indicative isotope at 367 (suggesting copper is present), may consist of $CsCu(CF_2)_2CF_3^+$.

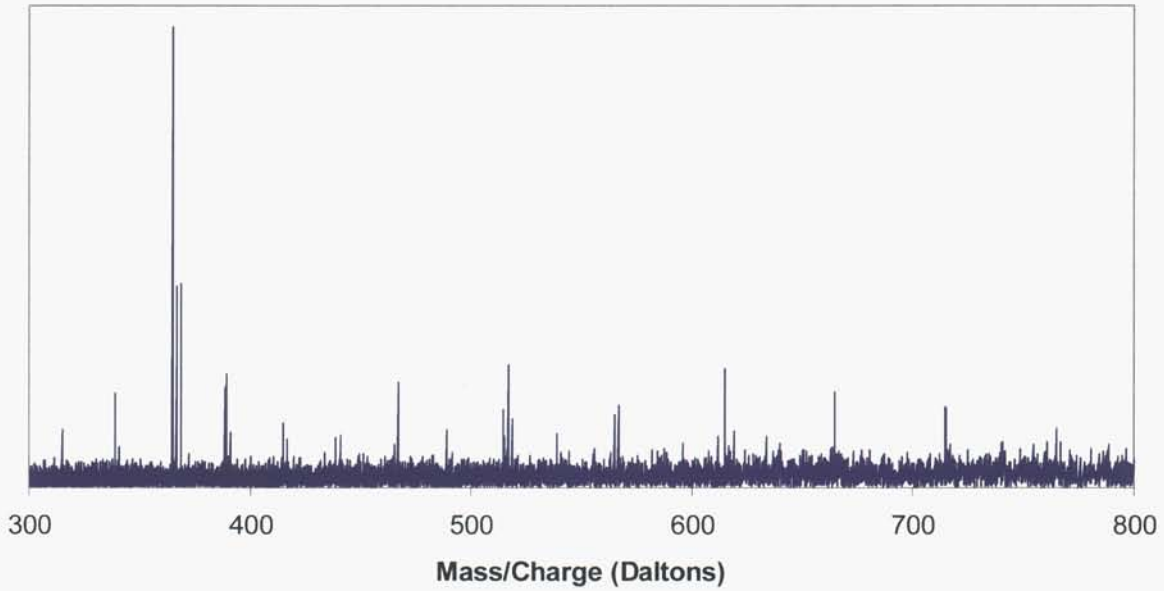

Figure 35. Signal from copper/cesium iodide in Teflon source.

3.4. Summary

An external laser desorption ion source was successfully installed on the existing Fourier transform ion-cyclotron resonance (FT-ICR) mass spectrometer. However, operation of this laser ablation source has only generated metal atom ions, no clusters have been found to date. It is believed that this is due to the design of the pulsed-nozzle/laser vaporization chamber. The final experimental configuration and design of the two source housings are described.

4. PROJECT SUMMARY

Small, well-defined platinum clusters have been prepared in zeolite hosts through ion exchange and controlled calcination/reduction processes. Several factors influence cluster size, particularly the zeolite structure, Pt-loading and calcination protocol employed. Zeolite-supported platinum clusters below 1 nm and with narrow size distribution have been prepared and characterized. To enable electrochemical application, the pores of the Pt-zeolite were filled with electrically-conductive carbon via infiltratation with carbon precursors, polymerization/cross-linking, and pyrolysis under inert conditions. A series of carbon precursors, and methods of pyrolysis, was investigated, with conductivity of the resultant carbon as the metric. Low-temperature pyrolysis of infiltrated furfuryl alcohol, followed by in-situ decomposition of propylene at 800 °C was chosen as the preferred method. While greater electrical conductivity is achievable at pyrolysis temperatures of ~ 1000 °C, Pt cluster sintering and collapse of porous structure result in an overall decrease in catalyst performance with such high-temperature pyrolysis. The presence of the carbonaceous matrix has been demonstrated to mitigate Pt cluster sintering on thermal treatment, with ramifications for fuel cells of enhanced durability. The zeolite host was removed by acid washing, to leave a Pt/C electrocatalyst possessing quasi-zeolitic porosity and Pt clusters of well-controlled size. Pt cluster sizes in the final electrocatalyst ranged from ~ 1.4 nm to ~ 5 nm, depending on the Pt loading, calcination protocol, and pyrolysis conditions employed. For Pt/C catalysts prepared under optimal conditions, characterization by TEM revealed narrow cluster size distributions, islands of lattice fringes for graphite (required for high electrical conductivity) and, in some cases, a regular microporous structure within the carbon (templated by the zeolite host).

These Pt/C materials had as much as 110 m^2/g_{Pt} electroactive surface area, an almost *30% improvement* over what is commercially available (86 m^2/g_{Pt}). These Pt/C materials also perform qualitatively as well as the ETEK material for the ORR, a non-trivial achievement. The fuel cell test showed that Pt/C outperformed the ETEK material by an *average of 50%* for a 300 hour test. Increasing surface area decreases the amount of Pt needed in a fuel cell, which translates into cost savings. Furthermore, the increased performance realized in the fuel cell test might ultimately mean less Pt is needed in a fuel cell; this again translates into cost savings. Finally, enhanced long-term stability is a key driver within the fuel cell community as improvements in this area must be realized before fuel cells find their way into the marketplace; these Pt/C materials hold great promise of enhanced stability over time.

An external laser desorption ion source was successfully installed on the existing Fourier transform ion-cyclotron resonance (FT-ICR) mass spectrometer. However, operation of this laser ablation source has only generated metal atom ions, no clusters have been found to date. It is believed that this is due to the design of the pulsed-nozzle/laser vaporization chamber. The final experimental configuration and design of the two source housings are described.

REFERENCES

(1) Boyen, H.-G.; Kästle, G.; Weigl, F.; Koslowski, B.; Dietrich, C.; Ziemann, P.; Spatz, J. P.; Riethmüller, S.; Hartmann, C.; Möller, M.; Schmid, G.; Garnier, M. G. and Oelhafen, P. Science 2002, 297 1533-1536.

(2) Cox, D. M.; Reichmann, K. C.; Trevor, D. J. and Kaldor, A. J. Chem. Phys. 1988, 88 (1), 111-119.

(3) Pan, Y. H.; Sohlberg, K. and Ridge, D. P. J. Am. Chem, Soc. 1991, 113 2406-2411.

(4) Riley, S. J. Clusters of Atoms and Molecules Ii, Haberland, H. E.; Springer Verlag: Berlin, 1994; 226.

(5) Xu, Z.; Xiao, F.-S.; Purnell, S. K.; Alexeev, O.; Kawi, S.; Deutsch, S. E. and Gates, B. C. Nature 1994, 372 346-348.

(6) Riley, S. J. and Parks, E. K. Proc. Of Advanced Research Workshop. NATO Advanced Study Institute, Richmond VA (U.S.A.), 1986; Jena;, P.; Rao;, B. K. and Khanna, S. N.; PLENUM PUBLISHING CORPORATION: 1987; 955.

(7) Vaarkamp, M.; Miller, J. T.; Modica, F. S.; Lane, G. S. and Koningsberger, D. C. 10th Int. Congr. Catal., 1993; Guczi, L., et al.; Elsevier: Amsterdam: 809-820.

(8) Kinoshita, K. J. Electrochem. Soc. 1990, 137 (3), 845-848.

(9) Andres, R. P.; Bielefeld, J. D.; Henderson, J. I.; Janes, D. B.; Kolagunta, V. R.; Kubiak, C. P.; Mahoney, W. J. and Osifchin, R. G. Science 1996, 273 (5282), 1690-1693.

(10) Pinna, N.; Maillard, M.; Courty, A.; Russier, V. and Pileni, M. P. Phys. Rev. B 2002, 66 045415.

(11) Alayan, R.; Arnaud, L.; Bourgey, A.; Broyer, M.; Cottancin, E.; Huntzinger, J. R.; Lermé, J.; Vialle, J. L.; Pellarin, M. and Guiraud, G. Rev. Sci. Instrum. 2004, 75 (7), 2461-2470.

(12) Judai, K.; Abbet, S.; Wörz, A. S.; Heiz, U. and Henry, C. R. J. Am. Chem. Soc. 2004, 126 2732.

(13) Hao, X. and Regalbuto, J. R. J. Colloid Interface Sci. 2003, 267 259.

(14) Miller, J. T.; Schreier, M.; Kropf, A. J. and Regalbuto, J. R. J. Catal. 2004, 255 203.

(15) Regalbuto, J. R.; Navada, A.; Shadid, S.; Bricker, M. L. and Chen, Q. J. Catal. 1999, 184 335.

(16) Schreier, M. and Regalbuto, J. R. J. Catal. 2004, 255 190.

(17) Hao, X.; Quach, L.; Korah, J.; Spieker, W. A. and Regalbuto, J. R. J. Mol. Catal. A: Chem. 2004, 219 97-107.

(18) Gallezot, P. Catal. Rev. Sci. Eng. 1979, 20 121.

(19) Homeyer, S. T. and Sachtler, W. M. H. J. Catal. 1989, 117 (1), 91.

(20) Homeyer, S. T. and Sachtler, W. M. H. J. Catal. 1989, 118 (1), 266.

(21) Jacobs, P. A. Stud. Surf. Sci. Catal. 1986, 29 357.

(22) De Graaf, J.; Van Dillen, A. J.; De Jong, K. P. and Koningsberger, D. C. J. Catal. 2001, 203 307-321.

(23) Exner, D.; Jaeger, N.; Kleine, A. and Schulz-Ekloff, G. J. Chem. Soc. Faraday Trans. I 1988, 84 (11), 4097-4104.

(24) Gallezot, P.; Alarcon-Diaz, A.; Dalmon, J.-A.; Renouprez, A. J. and Imelik, B. J. Catal. 1975, 39 334-349.

(25) Rabo, J. A.; Schomaker, V. and Pickert, P. E. Proc. 3rd Int. Congr. Catal. 1965; Sachtler, W. M. H.; North-Holland: Amsterdam: 1264-1276.

(26) Serykh, A. I.; Tkachenko, O. P.; Borovkov, V. Y.; Kazansky, V. B.; Beneke, M.; Jaeger, N. I. and Schulz-Ekloff, G. Phys. Chem. Chem. Phys. 2000, 2 5647-5652.

(27) Coker, E. N.; Steen, W. A.; Kelly, M. J.; Abraham, I. C. and Miller, J. E. Prepr. Pap.-Am. Chem. Soc., Div. Fuel Chem. 2004, 49 (2), 681-682.

(28) Coker, E. N.; Steen, W. A.; Miller, J. E. and Miller, J. T. J. Am. Chem. Soc. 2005, submitted

(29) Helfferich, F. Ion Exchange, Mcgraw-Hill Series in Advanced Chemistry; 1962; 156.

(30) Fletcher, P. and Townsend, R. P. Zeolites 1983, 3 129-133.

(31) Knapp, C.; Obuchi, A.; Uchisawa, J. O.; Kushiyama, S. and Avila, P. Microp. Mesop. Materials 1999, 31 23-31.

(32) Schmidt, T.; Gasteiger, H.; Stab, G.; Urban, P.; Kolb, D. and Behm, R. Characterization of High-Surface Area Electrocatalysts Using a Rotating Disk Electrode Configuration. JOURNAL OF THE ELECTROCHEMICAL SOCIETY 1998, 145 (7), 2354-2358.

(33) Maillard, F.; Martin, M.; Gloaguen, F. and Leger, J. M. Oxygen Electroreduction on Carbon-Supported Platinum Catalysts. Particle-Size Effect on the Tolerance to Methanol Competition. Electrochimica Acta 2002, 47 (21), 3431-3440.

(34) Itoe, R. N.; Wesson, G. D. and Kalu, E. E. Evaluation of Oxygen Transport Parameters in H{Sub 2}So{Sub 4}-Ch{Sub 3}Oh Mixtures Using Electrochemical Methods. Journal of the Electrochemical Society 2000, 147 (7), 2445-2450.

(35) Mello, R. M. and Ticianelli, E. A. Kinetic Study of the Hydrogen Oxidation Reaction on Platinum and Nafion Covered Platinum Electrodes. Electrochimica Acta 1997, 42 (6), 1031-1039.

(36) Gojkovic, S. L.; Zecevic, S. K. and Savinell, R. F. O-2 Reduction on an Ink-Type Rotating Disk Electrode Using Pt Supported on High-Area Carbons. Journal of the Electrochemical Society 1998, 145 (11), 3713-3720.

(37) Gloaguen, F.; Convert, P.; Gamburzev, S.; Velev, O. A. and Srinivasan, S. Evaluation of the Macro-Homogeneous and Agglomerate Model for Oxygen Reduction in Pemfcs. Electrochimica Acta 1998, 43 (24), 3767.

(38) Jarek, R. L. and Thornberg, S. M. Hazards of Dichlorosilane Exhaust Deposits from the High-Temperature Oxide Process as Determined by Ft-Icr Mass Spectrometry. IEEE Transactions on Semiconductor Manufacturing 2001, 14 (1), 20-25.

(39) Senko, M. W.; Canterbury, J. D.; Guan, S. H. and Marshall, A. G. A High-Performance Modular Data System for Fourier Transform Ion Cyclotron Resonance Mass Spectrometry. RAPID COMMUNICATIONS IN MASS SPECTROMETRY 1996, 10 (14), 1839-1844.

(40) Loh, S. K.; Hales, D. A. and Armentrout, P. B. A Continuous Source for Production of Cold, Mass-Selected Transition Metal-Cluster Ions. Chemical Physics Letters 1986, 129 (6), 527-532.

(41) Milani, P. and Deheer, W. Improved Pulsed Laser Vaporization Source for Production of Intense Beams of Neutral and Ionized Clusters. Review of Scientific Instruments 1990, 61 (7), 1835-1838.

(42) Kaldor, A. and Cox, D. M. Hydrogen Chemisorption on Gas-Phase Transition-Metal Clusters. Journal of the Chemical Society Faraday Transactions 1990, 86 (13), 2459-2463.

(43) Vakhtin, A. and Sugawara, K. Sequential Attachment of Hydrogen Molecules to Niobium Cluster Cations. Chemical Physics Letters 1999, 299 (6), 553-560.

(44) Koszinowski, K.; Schroder, D. and Schwarz, H. Reactivity of Small Cationic Platinum Clusters. Journal of Physical Chemistry A 2003, 107 (25), 4999-5006.

(45) Maruyama, S.; Anderson, L. and Smalley, R. Direct Injection Supersonic Cluster Beam Source for Ft-Icr Studies of Clusters. Review of Scientific Instruments 1990, 61 (12), 3686-3693.

APPENDIX A

Electrochemical experiments were carried out to help guide the electrocatalyst synthesis efforts. The main example of this collaboration was to help determine the ultimate pyrolysis temperature. Increasing the pyrolysis temperature increases the conductivity of the carbon matrix, but it also increases the probability of Pt clusters sintering. The figure below shows how the conductivity of poly-[furfuryl alcohol] increases as it is pyrolyzed to higher temperatures (blue curve).

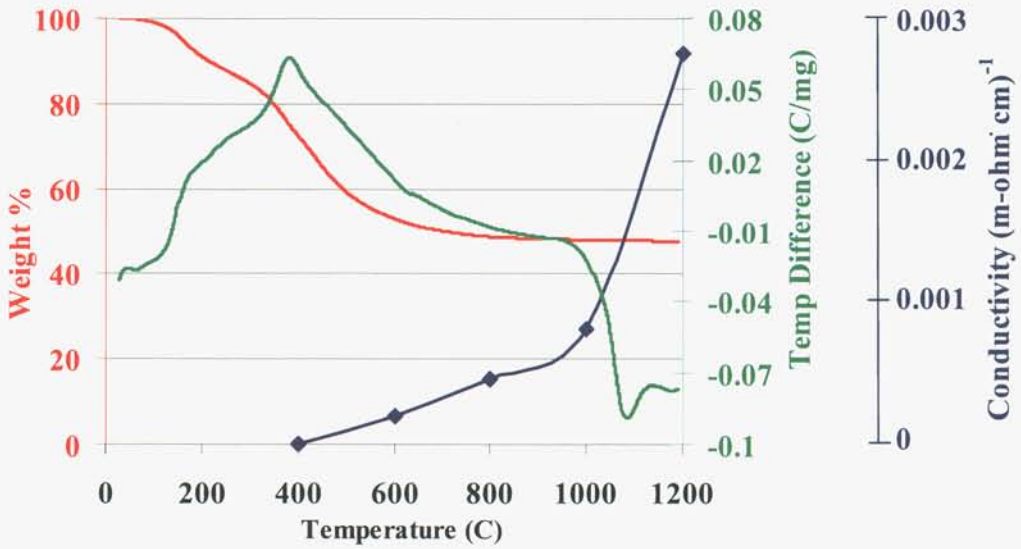

Overlaid on the figure above are data from a TGA experiment performed on pure poly-[furfuryl alcohol] in an inert gas flow. The inert gas ensures that all non-carbon polymeric material is burned off during the experiment. The red curve shows that weight loss from the poly-[furfuryl alcohol] is complete around 600°C, meaning only carbon remains. However, the conductivity has a marked increase at ~1000°C. Around this temperature, an endothermic temperature event (green curve) also occurs, lending evidence that the carbon is restructuring as it grows more conductive.

The above figure would lead one to conclude that the highest possible pyrolysis temperature should be used. This is not the case, however, because increasing the pyrolysis temperature also causes the Pt clusters to sinter. The XRD patterns presented in the next figure prove that increasing the pyrolysis temperature causes the Pt particles to grow, from 1.9nm at 500°C to 2.8nm at 1000°C. These diffraction patterns are for materials pyrolyzed at varying temperatures

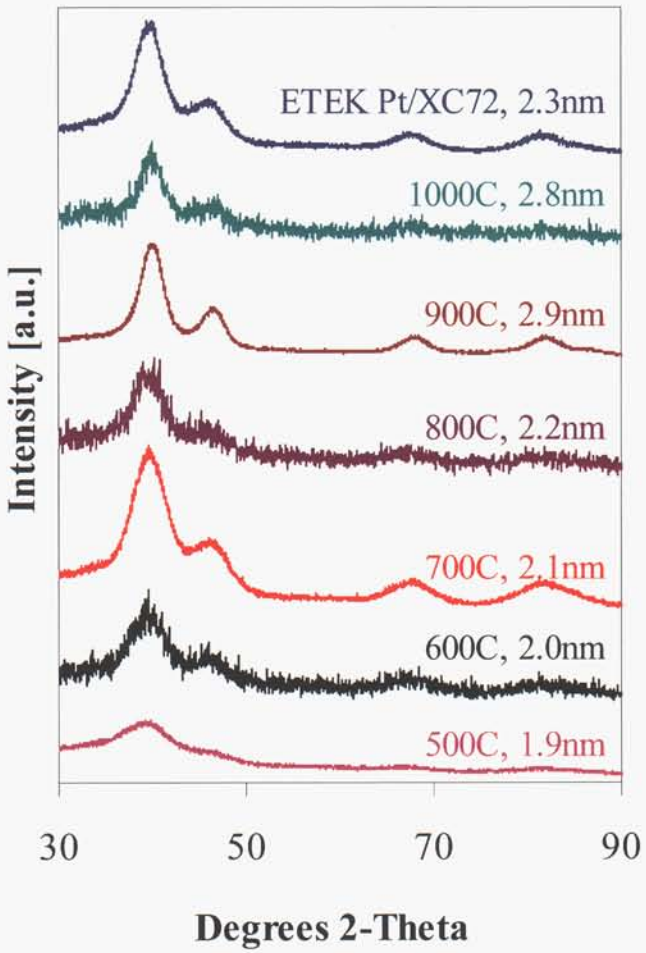

(shown in the figure) but all having a common "parent" calcined at 0.1°C/min and resulting in Pt/C electrocatalyst *ca.* 20 wt% Pt. An XRD pattern for the ETEK 20 wt% Pt on XC72 is also presented for comparison. To maintain particle sizes on the order of the ETEK standard, an 800°C pyrolysis temperature should not be exceeded. But, does this temperature yield a carbon matrix that is sufficiently conductive to produce an effective Pt/C electrocatalyst?

This question is answered and a compromise between particle sintering and conductivity is found by studying the ORR. Polarization curves for the same series of samples whose diffraction patterns are presented in the previous figure are shown below. The conditions of this experiment are the same as presented in the text of this report (*i.e.*, O_2 saturated 0.5M H_2SO_4, rotating disk electrode experiments, etc) and the rotation speed is 2000rpm. Clearly

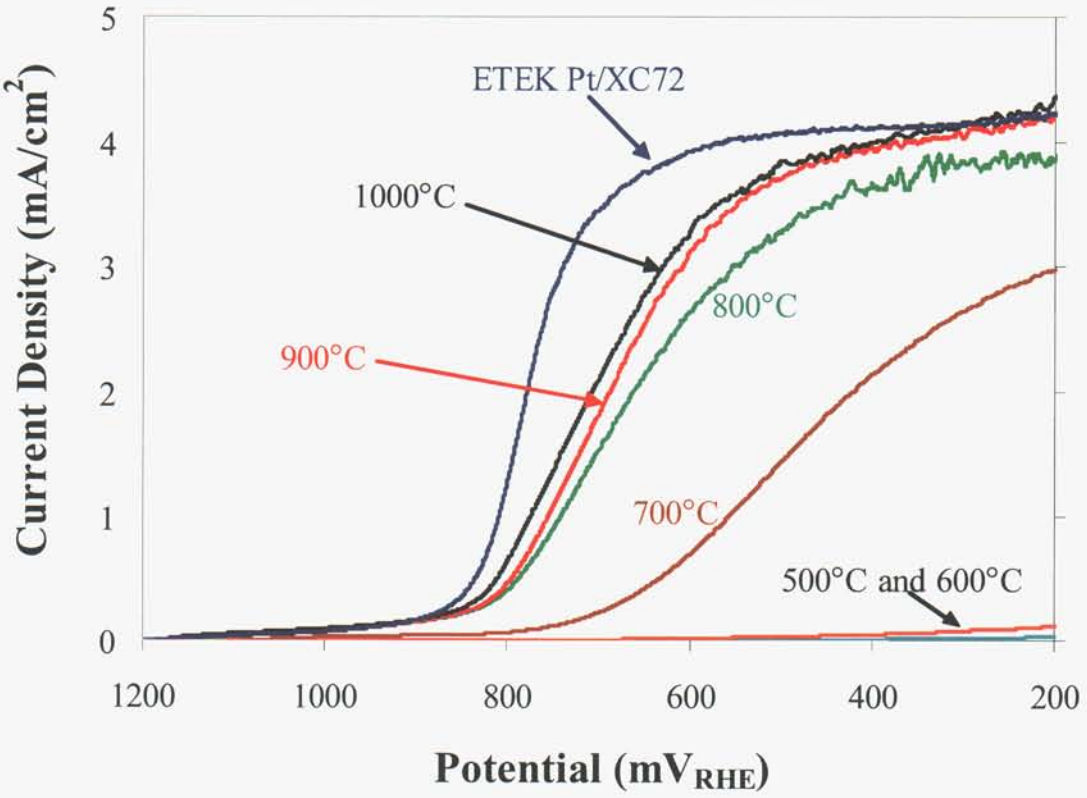

pyrolyzing to only 500°C or 600°C is not adequate. Even pyrolyzing to 700°C is likely not high enough, as the current only beings to increase at potentials ~700mV_{RHE}. Going to 800°C seems an ideal choice, as the additional increases to 900°C or 1000°C yield slightly enhanced performance (or higher currents at higher potentials) but likely not enough to justify the increases in cluster size (and subsequent loss of surface area). The ETEK 20 wt% Pt sample is shown for comparison. While this series of samples did not quite match the ETEK material's activity, the samples pyrolyzed to 800°C, 900°C and 1000°C are approaching the performance of this commercially available electrocatalyst.

It should be noted that CO stripping experiments were also performed on this series of samples. The 500°C, 600°C and 700°C samples failed to produce CO stripping events that could be integrated. The results for the remaining samples are shown below:

800°C	57.5 +/- 9.2 m^2/g_{Pt}
900°C	67.8 +/- 13.3 m^2/g_{Pt}
1000°C	66.0 +/- 12.8 m^2/g_{Pt}

APPENDIX B

Two figures are included in this Appendix. The first is a figure comparing ORR polarization curves for the series of samples presented in the body of the report with varying calcination temperature ramp rates. The second figure contains ORR polarization curves for the series of samples with different Pt wt%; these samples were also discussed in the report. The experimental conditions are the same as those discussed in the report's main text. The first figure shows that there were not any discernable trends in qualitative performance of the ORR as a function of calcination temperature ramp rate. The second figure shows that, in general, the Pt/C samples with lower wt% seem to qualitatively reduce oxygen more effectively. However, because of the additional film resistances (i_{film}), it is impossible to draw any quantitative conclusions. In fact, the lower weight percent samples likely have a higher O_2 concentration in the porous carbon matrix because of the larger volume fraction of carbon versus Pt; this additional O_2 would result in larger currents.

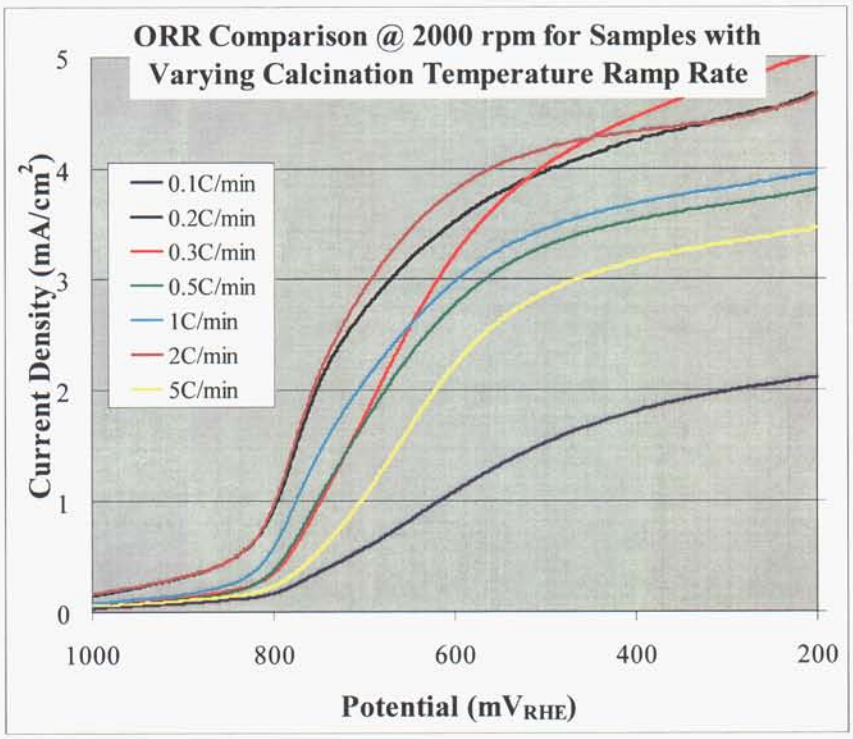

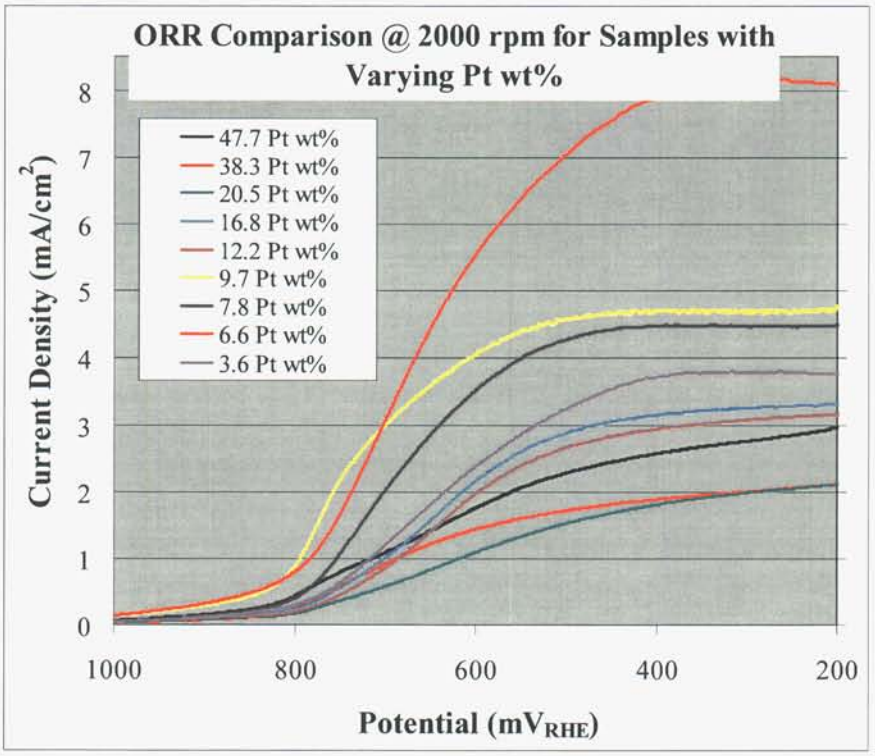
ORR Comparison @ 2000 rpm for Samples with Varying Pt wt%
47.7 Pt wt%
38.3 Pt wt%
20.5 Pt wt%
16.8 Pt wt%
12.2 Pt wt%
9.7 Pt wt%
7.8 Pt wt%
6.6 Pt wt%
3.6 Pt wt%
Current Density (mA/cm2)
0
1
2
3
4
5
6
7
8
1000
800
600
400
200
Potential (mVRHE)

APPENDIX C

Below is a typical cyclic voltammogram (CV) of one of the Pt/C materials compared to a Pt Black from ETEK. The CV was run in N_2 sparged 0.5M H_2SO_4 at 50mV/s. The Pt/C material was calcined at a ramp rate of 0.1°C/min, pyrolyzed to 600°C and the resulting Pt/C electrocatalyst had a ~50 wt% Pt. Glassy carbon electrodes were prepared as described in the text of the report, with a loading of $10\mu g_{Pt}$ for both the Pt/C material and ETEK's Pt Black. Note the H2 adsorption/desorption features around $-200mV_{Ag/AgCl}$, which is typical of polycrystalline Pt. The spike in current around $-250mV_{Ag/AgCl}$ is due to the evolution of H_2. Obviously, the Pt/C performs as expected.

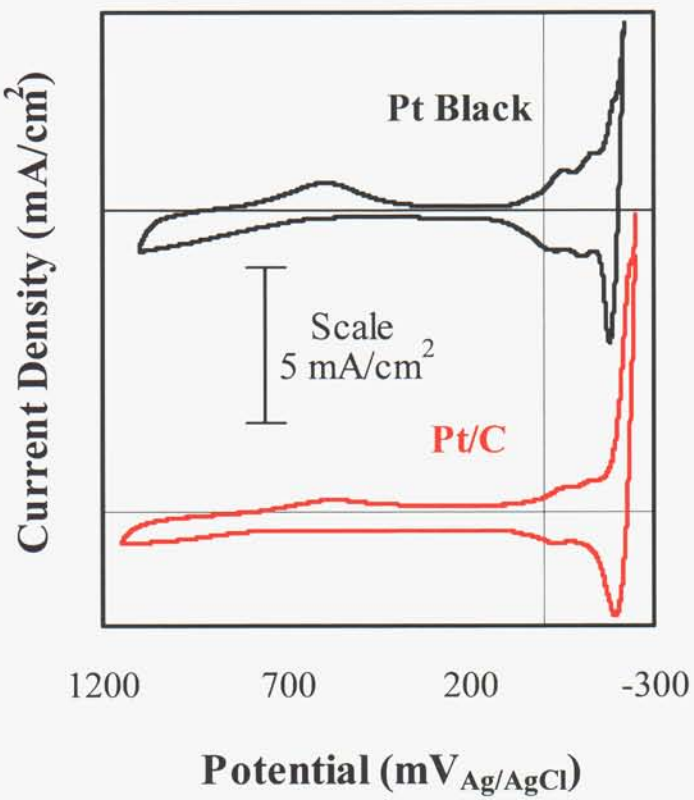

APPENDIX D

Attempts were made to synthesize Pt-Sn alloys. Work from the Bio micro-fuel cell grand challenge LDRD found that Pt-Sn alloys effectively catalyzed the oxidation of glucose, the fuel studied as part of that project. It is unclear whether the attempts to synthesize the Pt-Sn alloys following the methodologies in this LDRD were successful in producing Pt-Sn alloys, Pt-Sn bi-metallics, or if the Sn ion exchanged into the zeolite host at all. In any case, polarization experiments were performed and are shown in the following figure. Compared to the two samples synthesized as part of this effort (52598/4-19C and 19D) are commercially available 20 wt% Pt on XC72 carbon, 20 wt% Pt-Ru on XC72 carbon, and 20 wt% Pt-Sn on XC72 carbon; all from ETEK. The experiments were performed on a RDE rotating at 500rpm in 52.5mM glucose. The Pt-Sn catalysts synthesized here did not oxidize glucose as efficiently as what is currently available. It should be noted that attempts to optimize the synthesis of the Pt-Sn alloy were not pursued; optimizing the synthesis process could have resulted in enhanced performance for the oxidation of glucose.

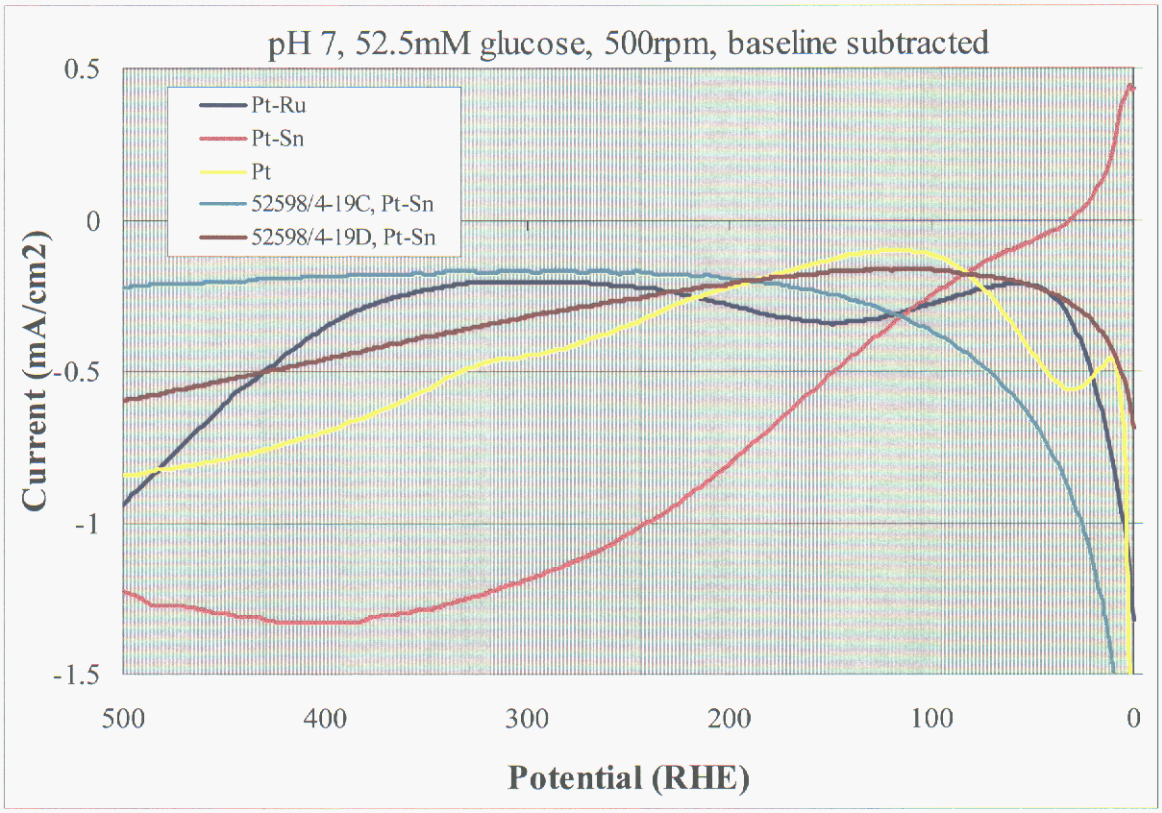

Distribution:

5	MS0889	S. M. Thornberg	01825
2	MS1349	E. N. Coker	01815
1	MS0888	W. A. Steen	01823
1	MS0778	R. L Jarek	06855
1	MS1349	J. E. Miller	01815
1	MS0889	J. W. Braithwaite	01825
1	MS1349	W. F. Hammetter	01815
1	MS0123	D. L Chavez	01011
2	MS9018	Central Technical Files	8945-1
2	MS0899	Technical Library	4536